Flavor diagonal nucleon charges using clover fermions on MILC HISQ ensembles

Sungwoo Park,[1,2,3,*] Rajan Gupta,[4,†] Tanmoy Bhattacharya,[4,‡] Fangcheng He,[4,§] Santanu Mondal,[5,‖] Huey-Wen Lin,[6,¶] and Boram Yoon[7,**]

[1]*Physical and Life Sciences Division, Lawrence Livermore National Laboratory, Livermore, California 94550, USA*
[2]*Nuclear Science Division, Lawrence Berkeley National Laboratory, Berkeley, California 94720, USA*
[3]*Thomas Jefferson National Accelerator Facility, 12000 Jefferson Avenue, Newport News, Virginia 23606, USA*
[4]*Los Alamos National Laboratory, Theoretical Division T-2, Los Alamos, New Mexico 87545, USA*
[5]*Ibsyn Scientific, 75C Park Street, Kolkata, India 700016*
[6]*Department of Physics and Astronomy, Michigan State University, East Lansing, Michigan 48824, USA*
[7]*NVIDIA Corporation, Santa Clara, California 95051, USA*

(Received 16 April 2025; accepted 26 August 2025; published 19 September 2025)

We present lattice results for the flavor diagonal charges of the proton from the analysis of eight ensembles generated using $2+1+1$-flavors of highly improved staggered quarks by the MILC Collaboration. The calculation includes all the needed connected and disconnected contributions to nucleon three-point function. For extracting matrix elements using fits to the spectral decomposition of these correlation functions, two strategies to remove excited state contributions are employed and compared. To renormalize these charges, the $2+1$-flavor mixing matrix is calculated in the regularization independent symmetric momentum subtraction intermediate scheme on the lattice. The final results are presented in the $\overline{\text{MS}}$ scheme at scale 2 GeV. The axial charges for the proton are $g_A^u = 0.781(25)$, $g_A^d = -0.440(39)$, and $g_A^s = -0.055(9)$; the tensor charges are $g_T^u = 0.782(28)$, $g_T^d = -0.195(16)$, and $g_T^s = -0.0016(12)$; and the scalar charges are $g_S^u = 9.39(88)$, $g_S^d = 8.84(93)$, and $g_S^s = 0.37(14)$. Results for the neutron are given by the $u \leftrightarrow d$ interchange. Results for the sigma terms are $\sigma_{\pi N}|_{\text{standard}} = 42(6)$ MeV from a "standard" analysis and $\sigma_{\pi N}|_{N\pi} = 61(6)$ MeV from an "$N\pi$" analysis that includes the contributions of multihadron $N\pi$ excited states as motivated by chiral perturbation theory. Our preferred value $\sigma_{\pi N}|_{N\pi}$ is consistent with the phenomenological extraction from $\pi - N$ scattering data. The strangeness content of the proton, for which the standard analysis is appropriate, is $\sigma_s|_{\text{standard}} = 35(13)$ MeV.

DOI: 10.1103/hn5v-9zgm

I. INTRODUCTION

Results for the flavor diagonal nucleon charges, $g_{A,S,T}^{u,d,s}$, are extracted from the matrix elements of axial, scalar, and tensor quark bilinear operators, $\bar{q}\Gamma q$ with the Dirac matrix $\Gamma = \gamma_\mu\gamma_5, I, \sigma_{\mu\nu}$, respectively, within ground state nucleons. The lattice QCD calculations were done using Wilson-clover fermions on eight ensembles generated by the MILC Collaboration with $2+1+1$-flavors of highly improved staggered quarks (HISQ) [1]. The lattice parameters used in this clover-on-HISQ calculation are given in Tables I and II.

The motivation for these calculations and much of the methodology used has already been published for g_A^q in Ref. [3], g_T^q in Ref. [4] and for the pion-nucleon sigma term, $\sigma_{\pi N} = m_{u,d} \times g_S^{u+d}$, in Ref. [5]. The charges $g_A^{u,d,s}$ give the contributions of the intrinsic spin of the quarks to the nucleon spin; the $g_T^{u,d,s}$ give the contribution of the quark electric dipole moment (EDM) operator to the nucleon EDM; and all three, $g_{A,S,T}^{u,d,s}$, give the coupling of dark matter

*Contact author: park49@llnl.gov
†Contact author: rajan@lanl.gov
‡Contact author: tanmoy@lanl.gov
§Contact author: fangchenghe@lanl.gov
‖Contact author: santanu.sinp@gmail.com
¶Contact author: hwlin@pa.msu.edu
**Contact author: byoon@nvidia.com

Published by the American Physical Society under the terms of the Creative Commons Attribution 4.0 International license. Further distribution of this work must maintain attribution to the author(s) and the published article's title, journal citation, and DOI. Funded by SCOAP³.

TABLE I. Lattice spacing a, valence pion mass M_π, gauge coupling β, Sheikholeslami-Wohlert coefficient $C_{\rm SW}$ defining the clover term in the Wilson action, light quark mass $am_{ud} = 1/2\kappa_{ud} - 4$, strange quark mass $am_s = 1/2\kappa_s - 4$, lattice volume $L^3 \times T$, and lattice size in units of M_π for the eight ensembles analyzed for flavor diagonal charges g_Γ^q.

Ensemble ID	a (fm)	M_π (MeV)	β	$C_{\rm SW}$	am_{ud}	am_s	$L^3 \times T$	$M_\pi L$
$a15m310$	0.1510(20)	320.6(4.3)	5.8	1.05094	−0.0893	−0.0210	$16^3 \times 48$	3.93
$a12m310$	0.1207(11)	310.2(2.8)	6.0	1.05094	−0.0695	−0.018718	$24^3 \times 64$	4.55
$a12m220$	0.1184(10)	227.9(1.9)	6.0	1.05091	−0.075	−0.02118	$32^3 \times 64$	4.38
$a09m310$	0.0888(8)	313.0(2.8)	6.3	1.04243	−0.05138	−0.016075	$32^3 \times 96$	4.51
$a09m220$	0.0872(7)	225.9(1.8)	6.3	1.04239	−0.0554	−0.01761	$48^3 \times 96$	4.79
$a09m130$	0.0871(6)	138.1(1.0)	6.3	1.04239	−0.058	−0.0174	$64^3 \times 96$	3.90
$a06m310$	0.0582(4)	319.6(2.2)	6.72	1.03493	−0.0398	−0.01841	$48^3 \times 144$	4.52
$a06m220$	0.0578(4)	235.2(1.7)	6.72	1.03493	−0.04222	−0.01801	$64^3 \times 144$	4.41

TABLE II. Parameters used in the calculation of the charges g_Γ^q on the eight ensembles. The second column gives the smearing parameter σ used in the creation of the covariant Gaussian smeared source for quark propagators. For ensemble $a06m220$, marked with (*), the connected contribution was done with $\sigma = 11$ while the disconnected was done with $\sigma = 9$. The list of source-sink time separations τ analyzed for the connected three-point functions is given in column three. The disconnected contributions were calculated for all τ and all intermediate t except on $a12m220$ for light quarks [$N^l_{\rm conf}$ marked with (#)]. On this ensemble, data were collected with fixed $t_{\rm skip} = 3$ and the four source time slices were fixed at $t_{src} = 2, 18, 34, 50$ rather than being chosen randomly. $N^{\rm 2pt}_{\rm conf}$ and $N^{\rm conn}_{\rm conf}$ give the number of configurations analyzed for two-point and connected three-point correlation functions, respectively. In the truncated solver with bias correction method, we used $N_{\rm LP}$ low and $N_{\rm HP}$ high precision measurements per configuration for the connected contributions. Columns 8–10 (11–13), specify the number of configurations, $N^l_{\rm conf}$ ($N^s_{\rm conf}$), analyzed for the light (strange) quark disconnected contributions with $N^l_{\rm src}$ ($N^s_{\rm src}$) Z_4 random noise sources and $N_{\rm LP}/N_{\rm HP}$ low to high precision measurements. In cases marked with (†), the $N^s_{\rm conf}$ configurations were split into two sets and analyzed with different number of sources $N^s_{\rm src}$, and the results averaged. Results for isovector charges on the full set of 13 configurations, including these, has been published in Ref. [2].

Ensemble ID	σ	τ/a	$N^{\rm 2pt}_{\rm conf}$	$N^{\rm conn}_{\rm conf}$	$N_{\rm LP}$	$N_{\rm HP}$	$N^l_{\rm conf}$	$N^l_{\rm src}$	$\frac{N^l_{\rm LP}}{N^l_{\rm HP}}$	$N^s_{\rm conf}$	$N^s_{\rm src}$	$\frac{N^s_{\rm LP}}{N^s_{\rm HP}}$
$a15m310$	4.2	$\{6,7,8,9\}$	1917	1917	64	8	1917	2000	50	1917	2000	50
$a12m310$	5.5	$\{8,10,12,14\}$	1013	1013	64	8	1013	10000	50	1013	8000	50
$a12m220$	5.5	$\{8,10,12,14\}$	959	744	64	4	958(#)	11000	30	870	5000	50
$a09m310$	7.0	$\{10,12,14,16\}$	2263	2263	64	4	1017	10000	50	1024	6000	50
$a09m220$	7.0	$\{10,12,14,16\}$	964	964	128	8	712	8000	30	847	10000	50
$a09m130$	7.0	$\{10,12,14,16\}$	1274	1290	128	4	1270	10000	50	994	10000/4000(†)	50
$a06m310$	12.0	$\{18,20,22,24\}$	977	500	128	4	808	12000	50	976	10000/4000(†)	50
$a06m220$	11.0/9.0 (*)	$\{18,20,22,24\}$	1010	649	64	4	1001	10000	50	1002	10000	50

or Higgs-like interactions with nucleons in the respective Lorentz channels. In addition, with $g_S^{u,d,s}$ in hand, we calculate the pion-nucleon sigma term, $\sigma_{\pi N} = m_{u,d} g_S^{u+d}$, and the strangeness content of the nucleon, $\sigma_s = m_s g_S^s$. We compare our results with those given in the latest Flavor Lattice Averaging Group (FLAG) report 2024 [6], a community review of calculations done until May 2024 by various lattice collaborations, and new results since then in Sec. VII.

This work supersedes our earlier publications [3–5] and updates in conference proceedings [7,8]. It includes a number of improvements:

(i) The calculation has been extended to eight ensembles described in Tables I and II. The point $a06m220$ is new.

(ii) The disconnected contributions on all ensembles except $a12m220$ have now been calculated with operator insertion at all intermediate points t between the nucleon source and the sink separated by Euclidean time τ.

(iii) The statistics on most of the ensembles have been increased.

(iv) Results for $g_S^{u,d,s}$ are new. In Ref. [5], the result for only the renormalization group invariant pion-nucleon sigma term, $\sigma_{\pi N} = m_{u,d} \times g_S^{u+d}$, was presented. Using the fact that $m\bar{\psi}\psi$ is the mass term in the action, implies $Z_m \times Z_S = 1$.

(v) Complete results for the renormalization of quark bilinears for the clover-on-HISQ formulation, i.e., the $2+1$-flavor mixing matrix, $Z_{A,S,T}$, are obtained nonperturbatively on the lattice using the regularization independent symmetric momentum subtraction (RI-sMOM) scheme [9,10]. These Zs are then matched to the $\overline{\rm MS}$ scheme and run to 2 GeV using

results from perturbation theory. Results in the basis $(u-d, u+d, s)$, most relevant to this work, are given in Appendix B. Our previous calculations used $Z_{\text{isoscalar}} \approx Z_{\text{isovector}}$, i.e., $Z_{\text{u+d}} \approx Z_{\text{u−d}}$ for the renormalization constants of the axial and tensor operators. Having completed the full calculation, we find removing this approximation has not changed the results significantly because the corrections are small as can be inferred from the numbers in Appendix B.

(vi) Resolving and removing the contributions of excited states to nucleon correlation function continues to be a leading systematic. These artifacts have to be removed to get ground state matrix elements. In our recent lattice QCD calculation of the nucleon axial vector form factor $G_A(Q^2)$ [11–13] and of the pion-nucleon sigma term $\sigma_{\pi N}$ [5], we presented evidence of larger-than-expected excited-state contributions (ESCs) from $N\pi$ and $N\pi\pi$ multihadron excited states in these nucleon three-point correlation functions. Motivated by these works, we study the impact of including $N\pi/N\pi\pi$ states in the analysis of all the flavor diagonal nucleon matrix elements.

For correlation functions with resolvable signal of ESCs, fits to get ground state matrix elements (GSMEs) now include two excited states in the spectral decomposition, and in each case compare fits with and without including the $N\pi$ excited state. These fits have been made using the full covariance matrix. To further control ESCs, we vary t_{skip}, the number of points skipped adjacent to the source and the sink, and the range of τ values included in the fits. For final results we take the average of these various fits, weighted by the Akaika information criterion (AIC) score [14].

(vii) The chiral-continuum-finite-volume (CCFV) extrapolation to the physical point, defined by $M_\pi \to 135$ MeV, $a \to 0$, and $M_\pi L \to \infty$, is done keeping the leading correction in each of the three variables.

This paper is organized as follows: a brief introduction to the lattice methods is given in Sec. II, and the strategies (models) used to remove excited state contributions are described in Sec. III. The averaging of models to get results for the charges using the AIC score is discussed in Sec. IV. The framework for obtaining the renormalized charges in the $\overline{\text{MS}}$ scheme at 2 GeV is described in Appendix B. The lattice calculation of the renormalization factors for the $2+1$-flavor theory is done using the RI-sMOM scheme. The extrapolation of the renormalized data to the physical point using the CCFV fits is discussed in Sec. VI. A comparison with previous results and our conclusions are given in Sec. VII.

II. LATTICE METHODOLOGY

The charges $g_{A,S,T}^{u,d,s}$ are extracted from the forward matrix elements of the flavor diagonal quark bilinear operator,

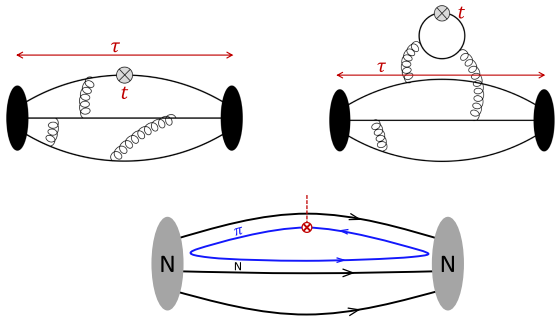


FIG. 1. Top row: connected (left) and disconnected (right) diagrams that contribute to the three-point functions from which the matrix element of flavor diagonal operators are extracted. The black and gray blobs denote the nucleon source and sink separated by Euclidean time τ. The operator, shown by the symbol $\otimes$, is inserted at all intermediate times t between the nucleon source and sink points. The bottom diagram (redraw of the top right) illustrates why the disconnected contribution for the scalar operator with u and d flavors can have an enhanced contribution due to the $N\pi$-intermediate state.

$\mathcal{O}_\Gamma^q(x) = \bar{q}(x)\Gamma q(x)$ with $q \in \{u, d, s\}$, inserted with zero momentum at time t as illustrated in Fig. 1 using the relation

$$\langle n(s_f, \mathbf{p}=0)|\bar{q}\Gamma q|n(s_i, \mathbf{p}=0)\rangle = g_\Gamma^q \bar{u}(s_f)\Gamma u(s_i), \tag{1}$$

with $u(s)$ as the nucleon spinor. These matrix elements are obtained from the three-point functions

$$C_\Gamma^{3\text{pt}}(t;\tau) = \text{Tr}\left[\mathcal{P}\langle 0|\mathcal{N}(\tau, \mathbf{p}=0)\mathcal{O}_\Gamma^q(t, \mathbf{q}=0)\bar{\mathcal{N}}(0)|0\rangle\right], \tag{2}$$

where $\mathcal{P}$ is the spin projection defined in Ref. [15]. The interpolating operator $\mathcal{N}$ used to create/annihilate the nucleon at the source/sink time slices 0 and τ is

$$\mathcal{N}(x) = \epsilon^{abc}\left[u^{aT}(x)C\gamma_5 \frac{1\pm\gamma_4}{2} d^b(x)\right]u^c(x). \tag{3}$$

Here, $\{a, b, c\}$ are color indices and $C = \gamma_4\gamma_2$ is the charge conjugation matrix. The $\mathcal{N}$ is projected to zero momentum at the sink to get the forward matrix elements. Henceforth, we will drop the momentum indices as $\mathbf{p} = \mathbf{q} = 0$ for all the calculations presented here. The goal is to design better $\mathcal{N}$, and increase the statistical precision so that there is good signal at large enough t and $\tau - t$ such that the extracted matrix elements are within the nucleon ground state. Otherwise ESCs have to be removed using fits to the spectral decomposition of the correlation functions as discussed in Sec. III.

The nucleon two- and three-point correlation functions are calculated using the Wilson-clover fermion action with the Sheikholeslami-Wohlert coefficient c_{SW} fixed to its

tree-level tadpole improved value, $c_{\rm SW} = 1/u_0^3$, where u_0 is the tadpole factor given by the fourth root of the plaquette expectation value calculated on HISQ lattices that have been hypercubic smeared [16].

Our calculation assumes isospin symmetry, i.e., $m_u = m_d \equiv m_l$, and the valence light quark mass m_l is tuned so that the clover-on-HISQ pion reproduces the HISQ-on-HISQ Goldstone (sea) pion mass $M_\pi^{\rm sea}$. The valence strange quark mass is tuned so that the clover-on-HISQ pseudoscalar meson mass reproduces $M_{s\bar{s}} = \sqrt{m_s^{\rm sea}/m_l^{\rm sea}} M_\pi^{\rm sea}$ [15], where $m_s^{\rm sea}/m_l^{\rm sea}$ is the ratio of HISQ (sea) quark masses and $M_\pi^{\rm sea}$ is fixed at the physical value 135 MeV [1]. While this clover-on-HISQ mixed action formulation is not unitary and could have an addition systematic uncertainty, no obvious effects have been observed in our calculations, presumably because taking the continuum limit matching the Goldstone pseudoscalar spectra of the clover and HISQ formulations is sufficient.

The quark propagators used to construct the quark line diagrams shown in Fig. 1 are the inverse of the clover Dirac operator with a smeared (Wuppertal gauge covariant Gaussian [17]) source. The smearing parameter σ is given in Table II and the same smearing is applied at the source and sink points. Efficacy of this smeared source in suppressing ESCs was explored in Refs. [18,19].

As illustrated in Fig. 1, the correlation function, $C_\Gamma^{\rm 3pt}(t;\tau)$ defined in Eq. (2), after Wick contractions, is the sum of two types of quark lines diagrams called "connected" and "disconnected":

$$C_\Gamma^{\rm 3pt}(t;\tau) = C_\Gamma^{\rm conn}(t;\tau) + C_\Gamma^{\rm disc}(t;\tau). \tag{4}$$

To reduce the computational cost, the connected diagrams are constructed using a coherent sequential source [18,20] and the truncated solver with bias correction [18,21,22] methods. The quark loop with zero-momentum operator insertion, i.e., $\mathbf{q} = \mathbf{0}$, for the disconnected contribution, $C_\Gamma^{\rm disc}$, is estimated stochastically using Z_4 random noise sources. This calculation was accelerated with a combination of the truncated solver with bias correction method [15], and the hopping parameter expansion used as a preconditioner [15,23,24]. For the scalar case, the disconnected contribution is calculated using the vacuum subtracted operator $\mathcal{O}_S^q - \langle \mathcal{O}_S^q \rangle$ [25]. Additional details are given in Ref. [15]. The statistics for the connected and disconnected calculations are given in Table II.

The calculation of the quark propagators and their contractions to construct correlation functions was done using the Chroma software suite [26]. On graphical processing units nodes, we use the QUDA library [27–29] with the multigrid invertor [30–32] built into it [33].

In our previous works [3,4], the removal of excited-state contributions (ESC) was carried out by making separate fits to $C_\Gamma^{\rm conn}(t;\tau)$ and $C_\Gamma^{\rm disc}(t;\tau)$. Similarly, the chiral-continuum (CC) extrapolations of $g_\Gamma^{q,\rm disc}$ and $g_\Gamma^{q,\rm conn}$ to $a \to 0$ and $M_\pi \to 135$ MeV were performed independently. This procedure may have introduced an unquantified systematic bias as discussed in Ref. [3]. This systematic has been removed in this work by making ESC fits to the sum and the subsequent CCFV extrapolation of the renormalized charges g_Γ^q. To understand the size of possible systematics in our previous work, we obtained results (ESC fits and CCFV extrapolation) both ways, and find the differences to be smaller than the statistical errors.

III. STRATEGIES TO REMOVE EXCITED-STATE CONTRIBUTIONS

The GSME $\langle 0|O_\Gamma^q|0\rangle$, and from them $g_\Gamma^{q;\rm bare}$ using Eq. (1), are extracted from fits to the spectral decomposition of the spin-projected $C_\Gamma^{\rm 3pt}(t;\tau)$, as follows:

$$C_\Gamma^{\rm 3pt}(t;\tau) = \sum_{i,j=0} \mathcal{A}_i^* \mathcal{A}_j \langle i|O_\Gamma^q|j\rangle e^{-M_i t - M_j(t-\tau)}. \tag{5}$$

The challenge lies in removing all ESCs since, even in our highest statistics ensembles, the right-hand side of Eq. (5) is truncated at three states. While the ESCs decrease exponentially with the mass gap ΔM and source-sink separation τ as $e^{-\Delta M \tau}$, the signal-to-noise ratio for $C_\Gamma^{\rm 3pt}$ degrades even faster exponentially as $e^{-(M_N - 3/2M_\pi)\tau}$ [34,35]. The $C_\Gamma^{\rm 3pt}$ are well measured only up to source-sink separation $\tau \approx 1.4$ fm and for $\tau \lesssim 1.4$ fm, ESCs are found to be significant. Three-state fits to remove these using Eq. (5) with $\mathcal{A}_0$, M_i and the $A_i^* A_j \langle i|O_\Gamma^q|j\rangle$ left as free parameters are not stable with current statistics. Additional information on these parameters is needed.

To make robust fits to Eq. (5), the key parameters are the ground state amplitude $\mathcal{A}_0$ and the finite volume spectrum M_i. If these are known *a priori*, then to extract $\langle 0|O_\Gamma^q|0\rangle$ only the combinations $A_i^* A_j \langle i|O_\Gamma^q|j\rangle$ involving the excited states remain as free parameters. This then becomes a tractable problem. Note, these $A_i^* A_j \langle i|O_\Gamma^q|j\rangle$ are not used in any subsequent analysis.

In principle, the $\mathcal{A}_0$ and M_i can be obtained from fits to the spectral decomposition of the two-point function, as follows:

$$C^{\rm 2pt}(\tau) = \sum_{i=0}^{3} |\mathcal{A}_i|^2 e^{-M_i \tau}. \tag{6}$$

To make n-state fits to $C_\Gamma^{\rm 3pt}(t;\tau)$ with input from $C^{\rm 2pt}(\tau)$, we need $C^{\rm 2pt}(\tau)$ truncated to $n+1$ (or higher) number of states presuming that the effects of all the neglected states are subsumed in the parameters of the $n+1$ (and higher) state. Of these, M_1 is the most important for controlling ESCs in fits to $C_\Gamma^{\rm 3pt}(t;\tau)$ with the contamination falling

exponentially with the mass gap. Unfortunately, with current statistics, four-state fits to Eq. (6) give large regions of parameter space with roughly the same χ^2/dof. We, therefore, resort to using physics motivated priors to determine the M_i.

The second challenge is that fits to $C^{2\text{pt}}(\tau)$ do not expose multihadron (such as $N\pi$, $N\pi\pi, \ldots$) excited states. The reason is that the coupling of multihadron states with nucleon quantum numbers to $\mathcal{N}$ is suppressed by factors of $1/L^3$ for each extra state [36]. On the other hand, as discussed later, their contribution to the matrix elements of certain operators is enhanced and compensates for the volume suppression. Therefore, in cases with enhanced contributions, these states need to be included in fits to $C^{3\text{pt}}_\Gamma(t;\tau)$ because the mass of $N(1)\pi(-1)$ [or $N(0)\pi(0)\pi(0)$] state is about 1230 MeV, which is significantly smaller than the first radial excitation $N(1440)$. In short, our first goal is to determine all the excited states, i.e., their M_i, that make significant contributions.

Our overall approach consists of making simultaneous fits to $C^{2\text{pt}}(\tau)$ (truncated at four states) and $C^{3\text{pt}}_\Gamma(t;\tau)$ (truncated at two or three states) within a single elimination jackknife process using binned data.[1] All fits are made using the full covariance matrix with respect to the time slices included in the fits. It is, however, restricted to being block diagonal for simultaneous fits to the two- and three-point correlation functions as the off-diagonal elements between them are not well determined with the current statistics.

We also carried out separate fits to the two- and three-point functions and the two sets of results overlap. No anomalous case showing a bias in the simultaneous fits was found. Since the simultaneous fits give more conservative errors and are better motivated as a method, the results are presented using them.

In fits without priors, or wide priors, the A_i and M_i are predominantly fixed by $C^{2\text{pt}}(\tau)$, while the $C^{3\text{pt}}_\Gamma(t;\tau)$ give $A^*_i A_j \langle i|O^q_\Gamma|j\rangle$ including the GSME $\langle 0|O^q_\Gamma|0\rangle$. In this case the priors are used mainly to stabilize the fits. The drawback, with current statistics, is that there is a whole region in the $\{A_i, M_i\}$ space that gives fits to $C^{2\text{pt}}(\tau)$ with similar χ^2/dof. Thus, there is considerable range of plausible values for M_1 with the lowest, theoretically, being the $N(1)\pi(-1)$ or $N(0)\pi(0)\pi(0)$. One way to reduce this uncertainty is to input physically motivated values of the M_i through narrow priors.

Ideally, one wants a data driven analysis procedure, i.e., the data and the fit should fix the M_i. With the current statistics, we are not able to achieve this desired situation. We, therefore, carry out the full analysis using two physically motivated but different values for M_1:

(1) The standard fit to $C^{2\text{pt}}(\tau)$ and $C^{3\text{pt}}(t;\tau)$ employs wide priors for all excited-state amplitudes, $\mathcal{A}_i$, and masses, M_i. In these simultaneous fits, the priors are used only to stabilize the fits. The A_0 and M_i, are mainly constrained by $C^{2\text{pt}}(\tau)$. The value of M_1 found in this case is $\gtrsim$1.5 GeV. This simultaneous fit is labeled "$\{4\}$" and M_1 is loosely identified with the radial excitation $N(1440)$.

(2) The $N\pi$ fit uses a narrow prior for M_1, centered on the noninteracting energy of the lowest allowed, $N(1)\pi(-1)$ or $N(0)\pi(0)\pi(0)$, lattice state on that ensemble. In practice, the energies of these two states are very similar, so they can be considered as one in Eq. (6) with a combined amplitude given by the sum. Throughout this work, for brevity we use the label $N\pi$ for their combined contribution. The priors for the other states are the same as in the standard fit. This fit is labeled "$\{4^{N\pi}\}$."

Since the two fit strategies are not distinguished by the χ^2, we explain, when quoting the final results, the physics motivations for the choices made. Also, where appropriate, we quote the difference as an estimate of an associated systematic uncertainty. Further details of our implementation of these two fits strategies are given in Refs. [5,12].

It is important to note that the mass of the $N\pi$ or the $N\pi\pi$ state decreases below that for the first radial excitation $N(1440)$ only for ensembles with $M_\pi \lesssim 200$ MeV, reaching $\sim$1230 MeV for physical pion mass ensembles. Thus, in cases with enhanced matrix elements, one expects to observe a strong dependence on M_π only for $M_\pi < 200$ MeV, which in our calculation leaves only the $a09m130$ ensemble. Fits to these data are shown in Figs. 2 and 3.

Furthermore, previous studies indicate that the difference in nucleon isovector axial and tensor charges, $g^{u-d}_{A,T}$, from the two strategies is small [12]. This is also observed for $g^{u,d,s}_{A,T}$ in this study, and the errors in results with the $N\pi$ strategy are comparable to the differences. Only for $g^{u,d}_S$ do the differences stand out. Thus, to nail down the best analysis strategy with up to three-state fits requires future higher statistics studies on more ensembles with $M_\pi \lesssim 200$ MeV.

To illustrate the difference in the values of M_1 coming out of the standard and $N\pi$ analyses, we quote the $a09m130$ values, which have the maximum difference. The Bayesian prior and width used for the mass gap $a\Delta M_1 = a(M_1 - M_0)$ is 0.35(20) for the standard and 0.12(2) for the $N\pi$ analysis with the central values

[1]The binning of the data is done in two steps. First, the $O(100)$ measurements made on each configuration are averaged. Second, these configuration averages are further binned using bin sizes ranging between two and nine resulting in 250–325 data points for the various ensembles. The autocorrelation function calculated using these binned data, which enter in the single elimination jackknife process, show no measurable correlations. Consequently, no augmentation of the single elimination jackknife errors is deemed necessary.

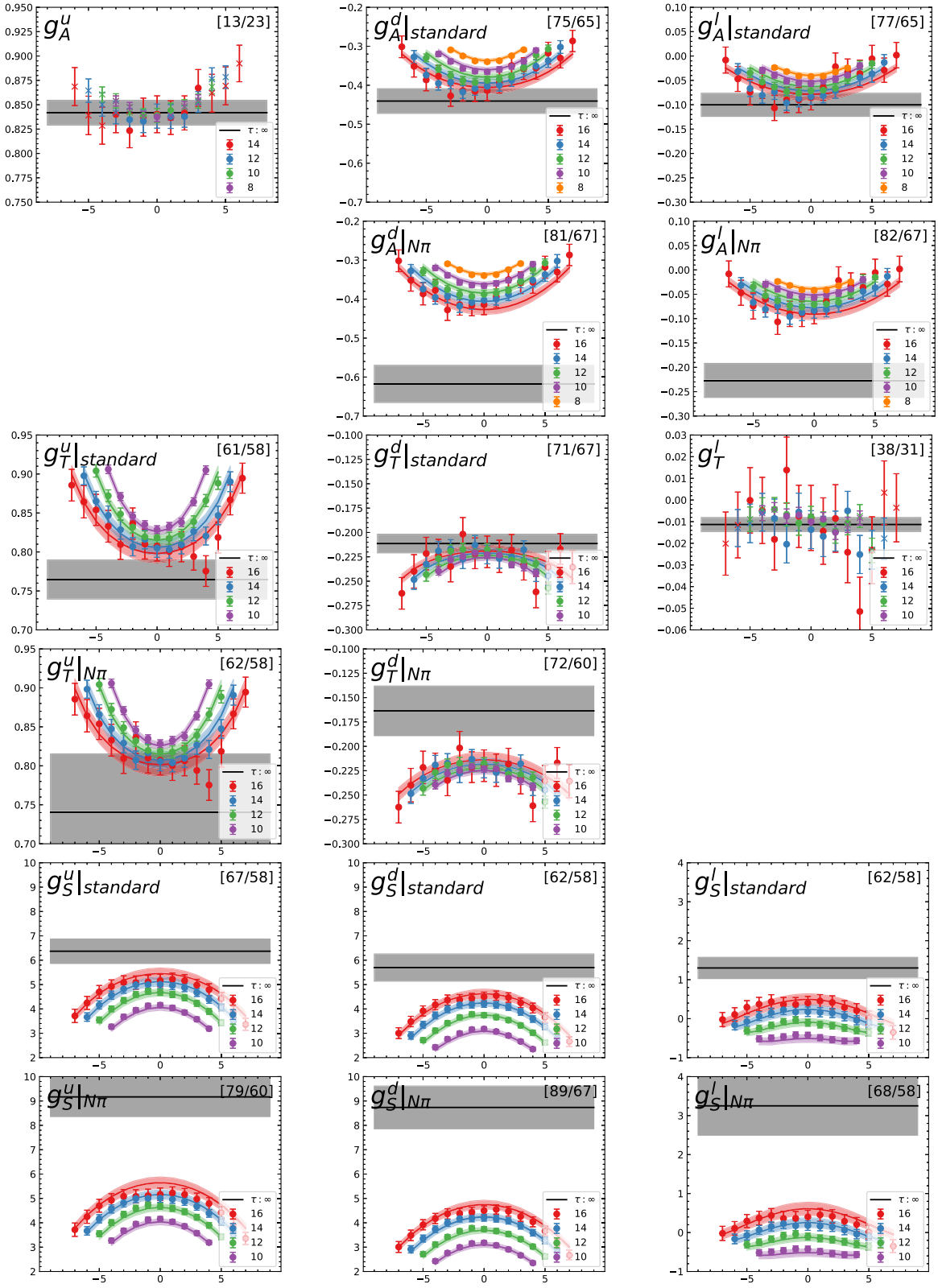


FIG. 2. Data for the bare charges $g^{u,d}_{A,T,S}$ (sum of the connected and disconnected contributions) obtained at various separations $\{\tau, t\}$ and plotted versus $(t-\tau/2)/a$ for the physical M_π ensemble $a09m130$. We show both the standard and $N\pi$ fits, defined in the text, when ESCs are manifest. In each case, the result of the fit is shown by lines of the same color as the data for the various τ/a listed in the label, and the $\tau \to \infty$ value is given by the gray band. We also show, for comparison, the light quark disconnected contributions, $g^l_{A,S,T}$, in the panels on the right and the ES fits to them. The χ^2/dof of the fit with the largest AIC score is given within square parenthesis in the top right corner.

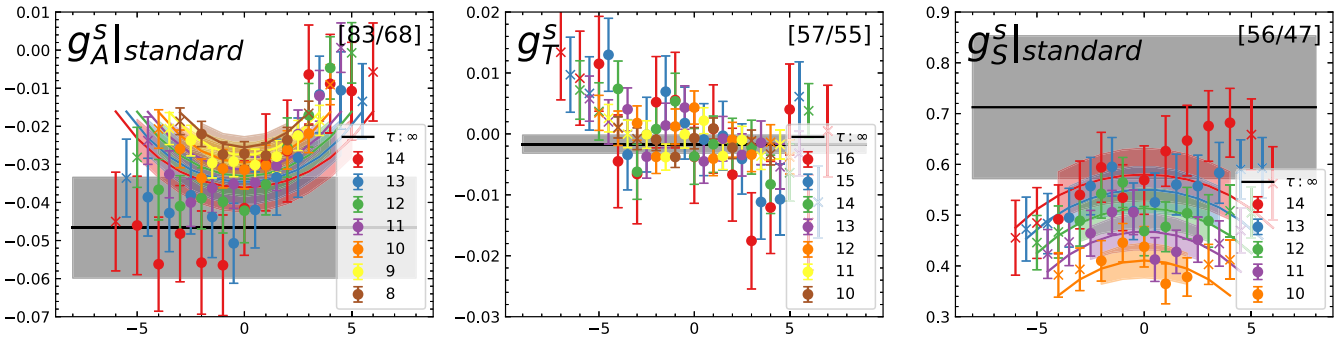


FIG. 3. Data for the bare strange charges, $g^s_{A,T,S}$, obtained at various separations $\{\tau, t\}$, and plotted versus $(t-\tau/2)/a$ for the physical M_π ensemble $a09m130$. These have only disconnected contributions. Only the standard fits to remove ESCs are shown and considered since the expected lowest multihadron state, ΣK, is heavier than the nucleon's radial excitation. Rest is the same as in Fig. 2.

corresponding to 0.79 GeV and 0.27 GeV in physical units, respectively. The output $a\Delta M_1$ from the simultaneous fits to $C^{2\text{pt}}$ and $C^{3\text{pt}}_\Gamma$ are consistent with the input priors, i.e., they lie in the range 0.24–0.30 for the standard and 0.11–0.14 for the $N\pi$ analysis. We note little dependence of output values on the quark flavor and/or the operator.

IV. MODEL AVERAGE OF VARIOUS FITS MADE TO REMOVE ESCS

We have carried out the following twelve ESC fits, i.e., the 12 "models," for both the standard and the $N\pi$ strategies to quantify change under variations of the fit parameters.

(i) The full list of τ values analyzed (covering 0.9–1.5 fm) is given in Table II. The ESC analysis is done with and without using the data with the largest τ. These largest τ data have the largest statistical but smallest systematic errors.

(ii) For each τ, we neglect data on τ_{skip} time slices next to the source and the sink that have the largest ESCs. Fits with three different t_{skip} values in the range of 0.2–0.4 fm were made.

(iii) The spectral decomposition of the three-point function, Eq. (5), is truncated at two states and three states. In all three-state fits, the $\langle 2|\mathcal{O}|2\rangle$ term is set to zero as it is not resolved by our data.

For the final results, we take the average weighted by the AIC score times the inverse of the variance, $\propto \exp[-(\chi^2 - 2N_{\text{dof}})/2]/\sigma^2$ [14,37]. In most cases, one set of values of τ and t_{skip} gives scores that are much higher than all others for both the two- and three-state fits. Thus, in practice, the model average is mainly over the variation of the result with the order of the truncation of Eq. (5). While most two- and three-state fits are similar, an example in the $N\pi$ analysis where we note a qualitative difference, even though the AIC scores were similar, is shown in Fig. 4. Since we do not expect an enhanced $N\pi$ state contribution to $g^q_{A,T}$, the large extrapolation in the two-state fit indicates that this is an artifact due to inadequate statistics. The large error and smaller extrapolation in the three-state fit is further indication that the data, in this and such cases, are statistics limited. More on this point in Sec. V.

Results from a two- versus three-state truncation of Eq. (5) highlight the tension between balancing systematic and statistical errors, which is accentuated in the $N\pi$ analysis. The two-state fit results may have significant systematic error from residual ESCs whereas the statistical precision of the data limits the robustness of the three-state fits. The same tension is also present between the fits with the two sets of τ values. The χ^2/dof or the AIC score or the p value of the fit, in most cases, does not distinguish between them. We regard cases with large extrapolation in the ESC fits or a large growth in errors or a large difference between two- and three-state fits as outliers due to inadequate statistics rather than a physical effect. The differences are, nevertheless, used to assign an appropriate systematic uncertainty in these cases.

V. PATTERN OF EXCITED-STATE CONTRIBUTIONS TO $g^{u,d,s}_{A,S,T}$

The $a09m130$ ensemble data for the ratio $C^{3\text{pt}}(t;\tau)/C^{2\text{pt}}(\tau)$ are shown in Figs. 2 and 3 as a function of the values of separations τ and current insertion time t simulated. As already stated above, we choose this physical pion mass ensemble to point out the notable features since the differences in ΔM_1 between the standard and the $N\pi$ analyses on it are the largest. In each panel, the final result, the AIC weighted average of the 12 ESC fits, the models, is shown by the horizontal gray band. The uncertainty bands on data points with a given color are obtained as follows: the value at each $\{\tau, t\}$ point is the weighted average of the 12 model values using the individual AIC weights, and the "error" is the spread. These points are then simply joined to form the bands. Note that these bands are not related in any simple way to the final gray band, but are presented to show the variation in the 12 values, which is given by the thickness of the bands.

Theoretically, the data for all τ must become symmetric about $t-\tau/2$ for the charges as the statistical precision

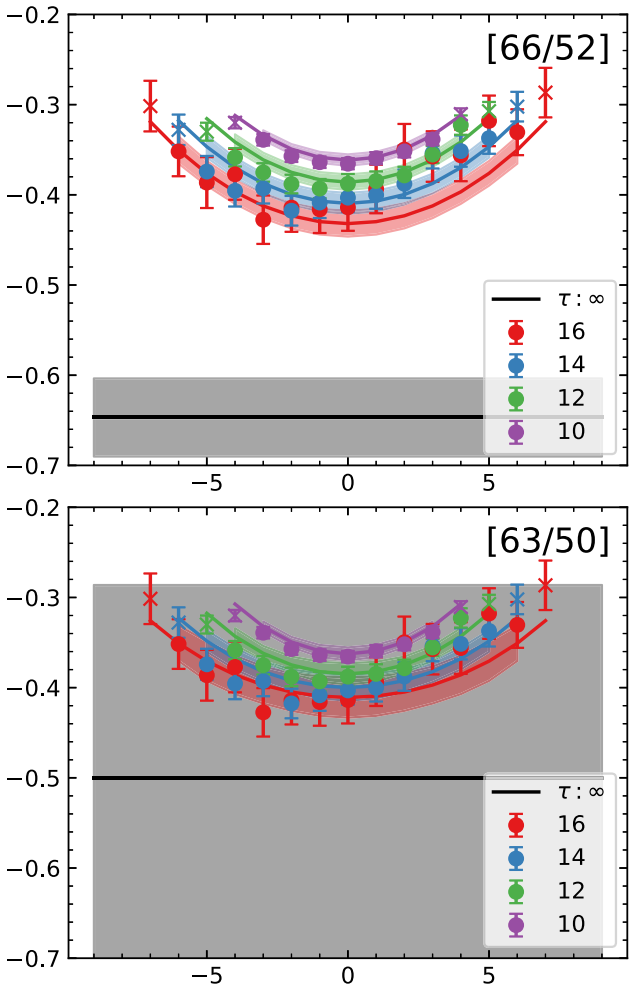


FIG. 4. Two panels showing the two-state (top) and three-state (bottom) $N\pi$ fit to the same data for g_A^d from the $a09m130$ ensemble. Points with $\tau = \{10, 12, 14, 16\}$ and $t_{\rm skip} = 2$ are included in the fits and are shown using filled circles. These two fits have the largest and similar AIC scores and dominate the model average, but differ qualitatively—the two-state fit shows a large extrapolation, while the three-state fit has a large error—and give different central values.

improves, and the convergence should become monotonic for large enough τ. Also, when choosing the $\tau_{\rm max}$ to use in the fits, the errors at that τ should ideally be small enough to resolve the differences in data at a given t but different τ. Clearly, for the physical mass ensemble $a09m130$, the data are already marginal by these criteria at $\tau/a = 14$ (≈1.2 fm).

In Refs. [3–5,12], we had studied the pattern of ESCs to $g^{u,d}_{A,S,T}$ separately for the connected and disconnected contributions. Figure 2 here shows fits to the sum, $C^{\rm conn}_\Gamma(t;\tau) + C^{\rm disc}_\Gamma(t;\tau)$. For completeness, we have compared these results for charges versus those obtained by doing separate fits to the connected and disconnected contributions, and find the differences are smaller than the errors. A summary of our observations is as follows:

(i) g_A^u: the convergence of the connected contribution is from below. The disconnected contribution is negative (~ -0.06) and converges to a more negative value as illustrated by $g_A^{l,s}$ in Figs. 2 and 3. A notable consequence is that the ESCs mostly cancel in the sum and the data at different τ overlap within the current statistical precision as illustrated for g_A^u in the top left panel in Fig. 2. We, therefore, estimate the $\tau \to \infty$ value by the weighted average of the data for a range of τ and t values, i.e., the "plateau method." Thus, the standard and the $N\pi$ results are the same.

(ii) g_A^d: the connected and disconnected contributions are both negative and their ESCs add in contrast to what is observed for g_A^u. We, therefore, perform two- and three-state fits to obtain the $\tau \to \infty$ value and the extrapolation is significantly larger in the $N\pi$ analysis.

(iii) g_A^l and g_A^s: the disconnected contribution is small and negative. The convergence is towards a more negative value for both as evident from Figs. 2 and 3.

(iv) g_T^u and g_T^d: the ESC contribution to g_T^u (g_T^d) is significant (small). The disconnected contribution is small (< 0.01) and negative. Thus, it only marginally reduces g_T^u and increases $|g_T^d|$. More important, the fits to g_T^u and g_T^d are good and the size of the extrapolation to the $\tau \to \infty$ value is small.

(v) g_T^l and g_T^s: the values are much smaller than the errors and there is no clear pattern of convergence. We, therefore, assume that there are no significant ESCs and make two fits to a constant *Ansatz*—with and without using the full covariance matrix. The results are consistent, however, the fit with the covariance matrix gives a larger error, and is chosen for the final result.

(vi) g_S^u and g_S^d: the connected and disconnected contributions to *both* are positive, the ESCs are large, and the convergence is from below. The size of the extrapolation in the $N\pi$ fits is large, giving larger values for $g_S^{u,d}$, which implies a larger pion-nucleon sigma term [5].

(vii) g_S^l and g_S^s: their values are also positive and significant, however, the errors in the current data are large. In one case, g_S^s from the $a09m310$ ensemble, only the diagonal elements of the covariance matrix were used since we did not find reasonable ranges of $\{\tau, t, t_{\rm skip}\}$ for which the off-diagonal elements were stable.

Results for the bare charges extracted using the two strategies to remove ESCs, and after model averaging, are summarized in Tables III–V. Their renormalization and conversion to the $\overline{\rm MS}$ scheme at the scale 2 GeV is done using the analysis for the $2+1$-flavor theory described in Appendix B.

TABLE III. Final bare axial charges $g_A^{u,d,s}$. These g_A^{u-d} results are obtained by doing the ES fit to the difference of the connected data with the insertion of the u and d quarks to take into account the correlations between the two. The g_A^u and g_A^d are extracted from a fit to the sum of the connected plus disconnected correlation functions. Their sum, $g_A^u + g_A^d$, can be compared to the result of a fit to the sum of the correlation functions, g_A^{u+d}. The errors are calculated using a single elimination jackknife method using data binned as described in the text, and each number is the AIC weighted average over the various model values. The results from the standard and $N\pi$ ESC fits are given separately.

Ensemble		g_A^{u-d}	g_A^u	g_A^d	g_A^{u+d}	g_A^l	g_A^s
a15m310	$\{3\}$	1.2416(57)	0.892(12)	−0.3538(57)	0.535(13)	−0.0431(28)	−0.0277(16)
	$\{3^{N\pi}\}$	1.2507(82)	0.892(12)	−0.3646(76)	0.516(16)	−0.0510(39)	−0.0315(22)
a12m310	$\{4\}$	1.267(11)	0.8896(97)	−0.372(24)	0.469(29)	−0.0696(77)	−0.0401(48)
	$\{4^{N\pi}\}$	1.2741(79)	0.8896(97)	−0.372(21)	0.479(20)	−0.0699(64)	−0.0420(27)
a12m220	$\{4\}$	1.285(30)	0.886(17)	−0.415(28)	0.457(43)	−0.083(16)	−0.049(13)
	$\{4^{N\pi}\}$	1.304(23)	0.886(17)	−0.441(28)	0.425(55)	−0.098(21)	−0.0595(72)
a09m310	$\{4\}$	1.256(45)	0.8695(87)	−0.3614(78)	0.506(14)	−0.0532(57)	−0.0304(25)
	$\{4^{N\pi}\}$	1.251(11)	0.8695(87)	−0.3688(85)	0.497(16)	−0.0578(66)	−0.0336(35)
a09m220	$\{4\}$	1.307(80)	0.8558(93)	−0.414(17)	0.441(24)	−0.084(15)	−0.0448(60)
	$\{4^{N\pi}\}$	1.318(33)	0.8558(93)	−0.436(25)	0.382(30)	−0.115(17)	−0.0620(85)
a09m130	$\{4\}$	1.281(32)	0.842(13)	−0.441(32)	0.386(46)	−0.100(24)	−0.047(13)
	$\{4^{N\pi}\}$	1.406(42)	0.842(13)	−0.618(48)	0.104(77)	−0.227(35)	−0.118(34)
a06m310	$\{4\}$	1.196(45)	0.870(31)	−0.372(23)	0.488(47)	−0.067(20)	−0.0396(49)
	$\{4^{N\pi}\}$	1.227(31)	0.862(29)	−0.379(18)	0.468(37)	−0.073(13)	−0.0429(55)
a06m220	$\{4\}$	1.256(32)	0.842(24)	−0.390(17)	0.434(34)	−0.079(15)	−0.0476(70)
	$\{4^{N\pi}\}$	1.271(32)	0.843(28)	−0.396(19)	0.426(38)	−0.094(26)	−0.0515(85)

TABLE IV. Final bare tensor charges $g_T^{u,d,s}$. The rest is the same as in Table III.

Ensemble		g_T^{u-d}	g_T^u	g_T^d	g_T^{u+d}	g_T^l	g_T^s
a15m310	$\{3\}$	1.1231(59)	0.902(12)	−0.2278(39)	0.669(11)	−0.0075(16)	−0.00204(54)
	$\{3^{N\pi}\}$	1.1096(80)	0.889(14)	−0.2211(47)	0.654(14)		
a12m310	$\{4\}$	1.0608(81)	0.827(25)	−0.2221(57)	0.601(34)	−0.00517(94)	−0.00188(55)
	$\{4^{N\pi}\}$	1.0509(96)	0.837(18)	−0.2219(52)	0.612(25)		
a12m220	$\{4\}$	1.062(13)	0.865(21)	−0.2087(92)	0.657(25)	−0.0046(23)	−0.0020(10)
	$\{4^{N\pi}\}$	1.039(28)	0.846(25)	−0.198(13)	0.648(36)		
a09m310	$\{4\}$	1.0288(47)	0.8210(84)	−0.2086(34)	0.6099(83)	−0.0056(10)	−0.00159(63)
	$\{4^{N\pi}\}$	1.033(19)	0.822(15)	−0.2080(45)	0.6030(95)		
a09m220	$\{4\}$	0.997(13)	0.791(15)	−0.2015(40)	0.568(26)	−0.0047(19)	−0.00178(69)
	$\{4^{N\pi}\}$	0.982(20)	0.773(21)	−0.1941(46)	0.538(39)		
a09m130	$\{4\}$	1.003(11)	0.765(25)	−0.2114(96)	0.528(29)	−0.0113(32)	−0.0017(15)
	$\{4^{N\pi}\}$	1.038(86)	0.741(74)	−0.164(25)	0.48(11)		
a06m310	$\{4\}$	0.985(15)	0.8005(68)	−0.2023(38)	0.5907(81)	−0.0057(14)	−0.00201(74)
	$\{4^{N\pi}\}$	0.962(31)	0.788(22)	−0.201(12)	0.581(26)		
a06m220	$\{4\}$	0.961(18)	0.757(20)	−0.186(10)	0.562(21)	−0.0058(16)	−0.00155(81)
	$\{4^{N\pi}\}$	0.933(34)	0.756(27)	−0.182(12)	0.557(27)		

The main question, in addition to the truncation of Eq. (5) to two- and three-state fits, is which analysis should be selected for the final values. In the $N\pi$ analysis, $M_1^{N\pi}$ is set to the noninteracting energy of the $N\pi$ state through a narrow prior and is not the output of a data driven fit. While the $N\pi$ state is expected to contribute in principle to all the charges (there is a contribution at one loop in chiral perturbation theory (χPT) [38]), no enhanced contribution

TABLE V. Final bare scalar charges $g_S^{u,d,s}$. The rest is the same as in Table III.

Ensemble		g_S^{u-d}	g_S^u	g_S^d	g_S^{u+d}	g_S^l	g_S^s
a15m310	$\{3\}$	0.829(24)	3.83(11)	3.068(87)	6.91(20)	0.648(77)	0.701(36)
	$\{3^{N\pi}\}$	0.829(31)	3.94(12)	3.26(12)	7.17(23)	0.761(70)	0.709(32)
a12m310	$\{4\}$	0.906(24)	4.64(23)	3.95(33)	8.54(54)	1.10(24)	0.694(80)
	$\{4^{N\pi}\}$	0.893(58)	4.57(15)	3.73(14)	8.28(28)	0.978(72)	0.671(47)
a12m220	$\{4\}$	1.037(88)	5.70(31)	4.53(22)	10.23(50)	1.15(23)	0.664(70)
	$\{4^{N\pi}\}$	1.13(11)	6.22(33)	4.98(28)	11.33(57)	1.53(25)	0.719(64)
a09m310	$\{4\}$	1.008(22)	4.47(14)	3.77(28)	8.10(34)	0.73(18)	0.499(57)
	$\{4^{N\pi}\}$	1.047(33)	4.73(21)	3.81(21)	8.55(43)	0.88(15)	0.597(82)
a09m220	$\{4\}$	1.008(31)	5.69(42)	4.68(43)	10.34(83)	1.19(38)	0.69(13)
	$\{4^{N\pi}\}$	1.001(62)	6.24(41)	5.18(41)	11.38(81)	1.53(30)	0.87(15)
a09m130	$\{4\}$	0.89(10)	6.37(50)	5.70(56)	12.0(1.0)	1.30(27)	0.71(14)
	$\{4^{N\pi}\}$	0.95(27)	9.17(81)	8.74(88)	17.5(1.5)	3.25(75)	1.11(30)
a06m310	$\{4\}$	1.180(70)	5.78(54)	4.53(43)	10.47(98)	0.99(15)	0.64(10)
	$\{4^{N\pi}\}$	1.258(89)	5.78(49)	4.59(36)	10.47(84)	1.12(16)	0.69(12)
a06m220	$\{4\}$	0.818(88)	6.15(61)	6.2(1.2)	12.8(1.7)	1.51(31)	0.520(96)
	$\{4^{N\pi}\}$	0.83(11)	6.19(57)	6.01(90)	12.7(1.4)	1.67(38)	0.62(20)

is expected except to the scalar charges [5] as evident from Fig. 2. Furthermore, ESCs from multihadron states, relative to those from the radial excitations, are expected to become significant only for $M_\pi \lesssim 200$ MeV, i.e., below which the $M_1^{N\pi}$ starts to be smaller than M_1^{radial}. Thus, to distinguish between the standard and $N\pi$ fits, we must rely on data close to the physical pion mass, i.e., in this work on only the $a09m130$ data shown in Figs. 2 and 3. With these caveats, our reasons for choosing the analysis strategy for presenting the final results for each of the charges are given below.

The error in the $\tau \to \infty$ extrapolated value for $g_A^{u,d}$ in the $N\pi$ analysis is large. For g_A^u, we see no significant ESCs, so the standard fit value is taken. In g_A^d, the ESCs to the connected and disconnected terms add and the $N\pi$ fit value is about 30% larger. We do not have a theoretical reason for such a large effect, nevertheless we take the average of the two estimates. Note, results for the isovector axial charge g_A^{u-d}, which has no disconnected contributions, are consistent with our final values already given in Ref. [13] as shown in Table IX.

In the case of $g_T^{u,d}$, the standard and $N\pi$ analyses give essentially the same central value and the extrapolation is small. Also, the ESCs to the connected and disconnected parts mostly cancel in g_T^d. The errors, however, are much larger, beyond what data would indicate, with the $N\pi$ fit. Since there is no phenomenological or χPT motivation for a large contribution from multihadron states in the tensor channel, we choose the standard analysis.

The $g_{A,T}^s$, illustrated in Fig. 3, get only disconnected contributions and the lowest multihadron state is likely to be ΣK as illustrated in Fig. 1). This is heavier than the radial excitation of the nucleon. Also, the data are noisy and the values are small. For these reasons we choose the standard analysis. It also gives an error estimate that we consider conservative.

The data for $g_S^{u,d}$ are the cleanest and the extrapolated values have reasonable errors. The two strategies, however, give different values but are not distinguished by the χ^2/dof. The size of the extrapolation is large in the $N\pi$ analysis and, on its own, calls into question even a three-state fit. However, χPT suggests such an enhanced contribution from the $N\pi$ and $N\pi\pi$ states as discussed in Ref. [5]. There we presented results for the pion-nucleon sigma term, $\sigma_{\pi N}$, and highlighted the ≈50% difference in $g_S^{u,d}$ from the two analysis strategies. The same reasoning leads us to continue to choose the $N\pi$ analysis in this work. Overall, our conclusion is that $g_S^{u,d}$ show large enhanced contributions from the $N\pi$ excited states unlike $g_{A,T}^{u,d}$. For g_S^s, the lowest multihadron state would again be the heavier ΣK, so no enhancement is expected with respect to the standard analysis.

Lastly, even though we have chosen the standard analysis values for $g_{A,S}^s$, we do show the CCFV extrapolation of the data from the $N\pi$ analysis in Figs. 10 and 16. The procedure for the renormalization of these charges is discussed in Appendix B.

VI. CHIRAL-CONTINUUM-FINITE-VOLUME EXTRAPOLATION AND ERROR BUDGET

The renormalized axial, $g_A^{u,d,s}$ and tensor, $g_T^{u,d,s}$ charges are extrapolated to the physical point, $a \to 0$,

$M_\pi = 135$ MeV, and $M_\pi L \to \infty$, using the *Ansatz*

$$g(a, M_\pi, M_\pi L) = c_0 + c_a a + c_2 M_\pi^2 + c_3 \frac{M_\pi^2 e^{-M_\pi L}}{\sqrt{M_\pi L}}, \quad (7)$$

that includes the leading corrections, pertinent to our lattice setup, in all three variables $\{a, M_\pi, M_\pi L\}$.

For the scalar charges g_S^u and g_S^d, chiral perturbation theory gives two differences. First, the chiral behavior, $g_S^{u,d} = d_0 + d_a a + d_1 M_\pi + d_2 M_\pi^2 + M_\pi^2 \log M_\pi^2 + \cdots$, starts with a term proportional to M_π [56]. Second, the contribution of $N\pi$ and $N\pi\pi$ excited states from higher order terms (chiral logs, etc.) is large as discussed in Ref. [5]. The difference on including these in ESC fits is shown in Fig. 2. Thus, one needs to include the higher order terms (chiral logs, etc.) in both fits to remove possibly large ESCs and in the chiral part of the CCFV *Ansatz*. Unfortunately, with data at only three values of M_π, only the first two terms, $\propto M_\pi$ and M_π^2 in addition to lattice spacing dependence, can be kept without overparametrization. Noting these points, the CCFV *Ansatz* used for the scalar charges $g_S^{u,d}$ is

$$g_S^{u,d}(a, M_\pi, M_\pi L) = d_0 + d_a a + d_2 M_\pi + d_3 M_\pi^2 + d_4 M_\pi \left(1 - \frac{2}{M_\pi L}\right) e^{-M_\pi L}. \quad (8)$$

Note that the finite-volume term is also modified [5]. For the strange scalar charge g_S^s, and for $g_{\{A,T\}}^s$, we do not expect a large contribution from pion loops since the lightest multihadron state is expected to be the much heavier ΣK. So we use the *Ansatz* given in Eq. (7).

The final results for the charges, after CCFV (or CC) extrapolations for the two strategies and the two renormalization methods, are summarized in Table VI. From these we obtain the final central values and the error budget given in Table VII. Adding errors in quadrature, the final results are given in Table VIII. We show, in Figs. 8–16 in Appendix A, only the CCFV fits but point out that the finite volume correction is small in all cases as can be inferred from the values given in Table VI. In panels showing CCFV fits versus M_π^2, the additional gray bands show fits keeping only the chiral corrections given in Eqs. (7) and (8). Overlap between these gray bands and the CCFV fits (pink bands), implies that the other two systematics, discretization and finite volume corrections are small. Overall, no significant finite-volume corrections are observed for $M_\pi L \gtrsim 4$.

Some specific observations on these CCFV fits to obtain the charges at the physical point are as follows.

A. Axial

CCFV fits in Figs. 8 and 9 for g_A^u and g_A^d, respectively, show similar large positive slope versus M_π^2, but with a

TABLE VI. Results for the flavor diagonal charges obtained after extrapolation to the physical point with and without finite volume corrections (the CCFV and CC fits). Results are presented for the two strategies (standard and $N\pi$) for removing ESCs and the two methods (Z_1 and Z_2, defined in Appendix B 4) for determining the renormalization constants. Note the tiny difference in g_T^s between the standard and $N\pi$ analysis since the mixing from light flavors depends on $N\pi$.

	Standard analysis for removing ESCs			$N\pi$ analysis		
q	g_A^q	g_T^q	g_S^q	g_A^q	g_T^q	g_S^q
Extrapolation excluding finite volume corrections (CC fit). Z_1 method						
u	0.803(17)	0.784(19)	6.35(56)	0.804(18)	0.776(28)	9.28(84)
d	−0.430(17)	−0.2001(65)	6.03(62)	−0.468(21)	−0.1903(87)	8.79(89)
s	−0.0539(64)	−0.00164(92)	0.457(95)	−0.0725(78)	−0.00165(92)	0.73(12)
Extrapolation excluding finite volume corrections (CC fit). Z_2 method						
u	0.779(18)	0.759(19)	6.32(57)	0.779(18)	0.747(29)	9.37(87)
d	−0.419(17)	−0.1939(68)	6.03(63)	−0.458(22)	−0.1830(91)	8.91(91)
s	−0.0543(69)	−0.0016(10)	0.41(10)	−0.0738(85)	−0.0016(10)	0.68(13)
Extrapolation including finite volume corrections (CCFV fit). Z_1 method						
u	0.784(22)	0.787(25)	6.36(56)	0.785(22)	0.776(37)	9.34(85)
d	−0.417(27)	−0.1957(93)	6.05(62)	−0.465(29)	−0.172(13)	8.81(91)
s	−0.0540(88)	−0.0016(11)	0.38(12)	−0.0705(95)	−0.0016(11)	0.66(16)
Extrapolation including finite volume corrections (CCFV fit). Z_2 method						
u	0.776(22)	0.778(26)	6.32(57)	0.778(22)	0.768(38)	9.38(88)
d	−0.414(27)	−0.1949(96)	6.04(63)	−0.462(29)	−0.171(13)	8.87(93)
s	−0.0554(94)	−0.0015(12)	0.36(13)	−0.073(10)	−0.0015(12)	0.66(17)

TABLE VII. Final results for the flavor diagonal charges obtained by combining the values given in Table VI using criteria specified in the text. The subscript CC denotes the systematic uncertainty assigned using the difference between the CCFV and CC fit values; and $N\pi$ for that between the standard and $N\pi$ strategies where appropriate. Values with the Z_1 and Z_2 renormalization methods (defined in Appendix B 4) are averaged. Results for g_A^q and g_T^q supersede those published previously in Refs. [3,4] and reproduced here.

	This work				PNDME 18 [3,4]	
q	g_A^q	g_T^q	$g_S^q\|_{N\pi}$	$g_S^q\|_{\mathrm{St}}$	g_A^q [3]	g_T^q [4]
u	$0.781(22)(11)_{\mathrm{CC}}$	$0.782(26)(11)_{\mathrm{CC}}$	$9.36(88)(4)_{\mathrm{CC}}$	$6.34(57)(1)_{\mathrm{CC}}$	0.777(25)(30)	0.784(28)(31)
d	$-0.440(29)(9)_{\mathrm{CC}}(24)_{N\pi}$	$-0.195(10)(2)_{\mathrm{CC}}(12)_{N\pi}$	$8.84(93)(1)_{\mathrm{CC}}$	$6.04(63)(1)_{\mathrm{CC}}$	−0.438(18)(30)	−0.204(11)(10)
s	$-0.055(9)(1)_{\mathrm{CC}}$	$-0.0016(12)(1)_{\mathrm{CC}}$	$0.66(17)(5)_{\mathrm{CC}}$	$0.37(13)(6)_{\mathrm{CC}}$	−0.053(8)	−0.027(16)

TABLE VIII. Final results for the flavor diagonal charges obtained by combining, in quadrature, the errors given in Table VII. The results for the axial charges, $g_A^{u,d}$, are the average over the $N\pi$ and standard analyses; the tensor, $g_T^{u,d}$, and the strange charges, $g_{A,S,T}^s$, are from the standard analysis; and $g_S^{u,d}$ are from the $N\pi$ analysis as explained in the text.

	Final results		
q	g_A^q	g_T^q	g_S^q
u	0.781(25)	0.782(28)	9.39(88)
d	−0.440(39)	−0.195(16)	8.84(93)
s	−0.055(9)	−0.0016(12)	0.37(14)

larger uncertainty in the $N\pi$ analysis. There also is a significant positive slope in g_A^u versus a but not in g_A^d. These variations decrease g_A^u and make g_A^d more negative as $a \to 0$ and $M_\pi \to 135$ MeV. They add in g_A^{u+d}, making it smaller, and almost cancel in g_A^{u-d}.

The CCFV estimates for g_A^u, summarized in Table VI, are, within errors, independent of the ESC strategy and the renormalization method. We, therefore, take the weighted average of the four values and the largest error to get $g_A^u = 0.781(22)$. To this we add a systematic uncertainty of 0.011 to account for the difference between the CCFV and CC values and quote $g_A^u = 0.781(22)(11)_{\mathrm{CC}}$ in Table VII.

Estimates of g_A^d are consistent between the two renormalization methods but ≈10% more negative with the $N\pi$ analysis. Based on the reasoning given in the extraction of the isovector axial form factors in Refs. [12,13], the $N\pi$ analysis is suggested, however, given the size of the errors, we defer choosing. So we take the mean and quote half the difference, 0.024, as a systematic uncertainty along with 0.009 for the difference between the CCFV and CC values. This gives $g_A^d = -0.440(29)(9)_{\mathrm{CC}}(24)_{N\pi}$.

For g_A^s, we choose the standard analysis as discussed previously and assign a systematic uncertainty only for the CCFV versus CC fits to get $g_A^s = 0.055(9)(1)_{\mathrm{CC}}$. These results for $g_A^{u,d,s}$, summarized in Table VII and VIII, are consistent with, and update those published in Ref. [3].

B. Tensor

The magnitude of ESCs in g_T^u is significant, while the errors in g_T^d and g_T^s are large, especially on the physical pion mass ensemble $a09m130$, as shown in Fig. 2 and in Ref. [4]. The CCFV fits are shown in Figs. 11–13. The standard and $N\pi$ analyses give consistent estimates but the errors in the $N\pi$ case are ≈50% larger. For all three charges, $g_T^{u,d,s}$, we average the values from the two renormalization methods and use the difference between CCFV and CC fits to assign a systematic uncertainty. Since no enhanced contributions from multihadron, $N\pi$, states is expected in the tensor channel, our choice is the standard analysis and the CCFV fits. Nevertheless, to be conservative and account for the $\approx 2\sigma$ difference between the standard and $N\pi$ values for g_T^d, we assign half the difference, 0.012, as an additional systematic uncertainty. The final results are summarized in Tables VII and VIII.

C. Scalar

The behavior of g_S^u and g_S^d versus a is similar and there is a significant negative slope, i.e., the value increases as $a \to 0$ as shown in Figs. 14 and 15. Similarly, the value increases as $M_\pi \to 135$ MeV. There is a significant difference between the standard and $N\pi$ fit values, and the extrapolation of the $N\pi$ data is large. The physical pion mass data point $a09m130$, therefore, plays a crucial role in the extrapolation. Results after CCFV extrapolation of the standard and $N\pi$ analyses data are given in Tables VI and VII. Based on the χPT analysis presented in Ref. [5], we pick the $N\pi$ analysis for the final values of $g_S^{u,d}$ given in Table VIII. Again, we choose the standard analysis value for g_S^s as the lowest multihadron state is expected to be ΣK.

D. The pion-nucleon sigma term $\sigma_{\pi N}$

Results for the renormalization group invariant pion-nucleon sigma term were presented in Ref. [5] where it was calculated on each ensemble using the bare quantities $\sigma_{\pi N} = m_l^{\mathrm{bare}} g_S^{u+d,\mathrm{bare}}$ and the data extrapolated to the physical point using the next-to-next leading order ($\mathrm{N^2LO}$) χPT expression [56]:

$$\sigma_{\pi N} = (d_2 + d_2^a a) M_\pi^2 + d_3 M_\pi^3 + d_4 M_\pi^4 + d_{4L} M_\pi^4 \log \frac{M_\pi^2}{M_N^2}. \tag{9}$$

The χPT analysis in Ref. [5] suggested that all five terms contribute significantly in a CC fit, and finite-volume corrections are less than 1 MeV for the physical pion mass ensemble $a09m130$. So we again present results from the CC extrapolation. With data at only three values of $M_\pi \approx 135$, 220, 310 MeV, we can include at most three chiral terms. The fit with the leading terms is shown in Fig. 17 (top). The bottom panels show the fit including the fourth chiral term, $\propto d_{4L}$, realized by fixing the coefficient d_3 to its χPT value, d_3^χ, evaluated with $M_N = 0.939$ GeV, $g_A = 1.276$, and $F_\pi = 92.3$ MeV [5]. Averaging these two values gives our updated results, $\sigma_{\pi N}|_{N\pi} = 61(6)$ MeV for the "$N\pi$" and $\sigma_{\pi N}|_{\text{standard}} = 41(6)$ MeV for the standard analysis, which overlap with those given in Ref. [5].

In this work, we also do the CCFV extrapolation of the renormalized charges g_S^{u+d} and $g_S^{u,d,s}$. Our preferred value for the isoscalar charge, g_S^{u+d}, is obtained by doing ESC fits to the sum of the total u and d correlators. The results are $g_S^{u+d} = 12.4(1.2)$ for the standard and $g_S^{u+d} = 17.8(1.6)$ for the $N\pi$ analysis. The value $g_S^s = 0.37(14)$ is, as explained before, taken from the standard analysis. Combining these with the renormalized quark masses $m_l = 3.427(51)$ and $m_s = 93.46(58)$ MeV given in the FLAG 2024 report [6] for the $N_f = 2+1+1$ theory, provides the second estimates: $\sigma_{\pi N}|_{N\pi} = 61(6)$ MeV for the $N\pi$ analysis, and $\sigma_{\pi N}|_{\text{standard}} = 43(4)$ MeV and $\sigma_s = 35(13)$ MeV from the standard analysis. Note that if the individual values of g_S^u and g_S^d are taken from Table VII, then $\sigma_{\pi N}$ is larger by about 2 MeV.

Averaging the two estimates for $\sigma_{\pi N}$ and taking the larger of the errors, our final values are

$$\begin{aligned} \sigma_{\pi N}|_{\text{standard}} &= 42(6)\ \text{MeV}, \\ \sigma_{\pi N}|_{N\pi} &= 61(6)\ \text{MeV}, \\ \sigma_s|_{\text{standard}} &= 35(13)\ \text{MeV}. \end{aligned} \tag{10}$$

These are summarized in Fig. 7 along with other lattice determinations with $2+1+1$ and $2+1$-flavor simulations that meet the FLAG criteria [6], and also the results for $\sigma_{\pi N}$ from phenomenology.

E. Extracting the isovector charges $g_{A,T,S}^{u-d}$

The disconnected contributions, which have large errors, cancel exactly in the isovector charges, $g_{A,T,S}^{u-d}$, for the isospin-symmetric theory. Thus, our overall strategy to get the isovector charges is to make excited-state (ES) fits to the difference of the connected contributions,

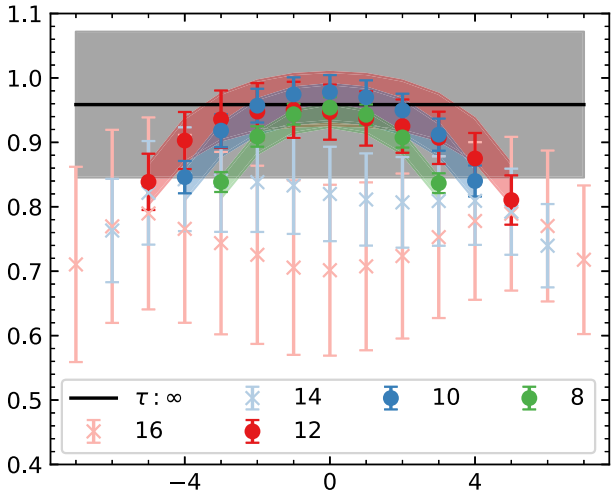


FIG. 5. Ratio plot for $g_S^{u-d,\text{bare}}$ on the a09m130 ensemble. The $\tau = \infty$ value is taken from the fit to $\tau = 8$, 10 and 12 data, which show no significant ESCs at $t = \tau/2$. The $\tau = 14$ and 16 data are neglected as, with current statistics, they have large errors and deviate from the expected behavior of monotonic convergence.

i.e., to $C_\Gamma^{u,\text{conn}}(t;\tau) - C_\Gamma^{d,\text{conn}}(t;\tau)$. These fits are much more robust compared to those for the individual flavor diagonal charges, and benefit from correlated fluctuations that are missed in the construction $g^{u,\text{bare}} - g^{d,\text{bare}}$. For example, extracting g_S^{u-d} from separate fits to the two $C_S^{\text{conn+disc}}(t;\tau)$ gives $O(1)$ errors with current data. This occurs for the two reasons illustrated by the $a09m130$ data in Fig. 5. First, the data for the larger τ ($\tau = 14$ and 16) do not satisfy the two conditions that must hold for fits to give consistent results—monotonic convergence from below and symmetry about $\tau/2$. These features are exhibited by the data from the other seven ensembles and we have checked that they improve with increasing statistical precision. Second, within errors, which increase rapidly with τ, the data around $\tau/2$ overlap for $\tau = 8$, 10, 12. This, ideally, indicates convergence by the plateau criteria, however, for confirmation much higher precision $\tau = 14$ and 16 data are needed. On the other hand, using two-state fits to remove residual ESCs is not well constrained.

Our final results for isovector charges from the full set of clover-on-HISQ calculations (using 13 data points on 11 HISQ ensembles, CCFV extrapolation, and taking the average of values with Z_1 and Z_2 renormalization) have already been published in Ref. [13]. For completeness, Table IX summarizes the values from this work using eight ensembles, standard and $N\pi$ analyses, CCFV and CC extrapolations; and the same two renormalization methods. The two sets of results are consistent, with the values obtained here having slightly larger errors. The only notable feature in both is the difference between the various estimates for g_A^{u-d} that has already been pointed out in Ref. [13].

TABLE IX. Results for the isovector charges with the two strategies, standard and $N\pi$, used to remove ESCs; the two methods, Z_1 and Z_2, used for renormalization; and the two *Ansätze*, CCFV and CC, used to extrapolate data to the physical point. The final values from this work are compared with the average of Z_1 and Z_2 values from Ref. [13] obtained with CCFV extrapolation of the full set of 13 clover-on-HISQ calculations. The CCFV extrapolations based on eight versus 13 points account for most of the differences between the results. The standard analysis strategy is labeled "3*" in Ref. [13], while the $N\pi$ analysis is similar to "3-RD."

	Standard analysis for removing ESCs				$N\pi$ analysis			
	This work (Z_1)	This work (Z_2)	This work	Ref. [13]	This work (Z_1)	This work (Z_2)	This work	Ref. [13]
$g_A^{u-d}\|_{\rm CC}$	1.284(29)	1.221(30)			1.328(26)	1.277(27)		
$g_A^{u-d}\|_{\rm CCFV}$	1.221(39)	1.206(40)	1.214(40)	1.240(27)	1.288(32)	1.278(33)	1.283(33)	1.294(49)
$g_T^{u-d}\|_{\rm CC}$	1.007(12)	0.969(12)			0.976(27)	0.929(28)		
$g_T^{u-d}\|_{\rm CCFV}$	1.010(16)	0.998(17)	1.004(17)	0.989(34)	0.976(36)	0.969(37)	0.973(37)	0.991(24)
$g_S^{u-d}\|_{\rm CC}$	0.99(11)	0.98(11)			1.17(27)	1.17(27)		
$g_S^{u-d}\|_{\rm CCFV}$	0.98(11)	0.96(12)	0.97(12)	1.022(100)	1.18(27)	1.17(28)	1.18(28)	1.085(115)

VII. COMPARISON WITH PREVIOUS RESULTS AND CONCLUSIONS

Our final results, which supersede those presented in Refs. [3,4], are summarized in Tables VII and VIII. The improvements made in this work are described in Sec. I. The FLAG 2024 report [6] quotes our previous results for $g_{A,T}^{u,d,s}$ (from Refs. [3,4]) as the FLAG values for $2+1+1$-flavor simulations. The updated versions of the FLAG summary figures, including data from other collaborations that meet the FLAG criteria for averaging, and post FLAG 2024 results from the ETM Collaboration [39], are shown in Figs. 6 and 7.

From the axial charges, $g_A^{u,d,s}$ given in Table VIII, we calculate the contribution of the intrinsic spin of quarks to the nucleon spins to be $0.5\Delta\Sigma_q = 0.5\sum_q g_A^q = 0.143(24)$. This is consistent with the COMPASS analysis $0.13 < 0.5\Delta\Sigma_q < 0.18$ evaluated at 3 GeV^2 [57].

The lattice determination of tensor charges, $g_T^{u,d,s}$, is far more accurate than extractions from the transversity distributions of quarks in semi-inclusive deep-inelastic

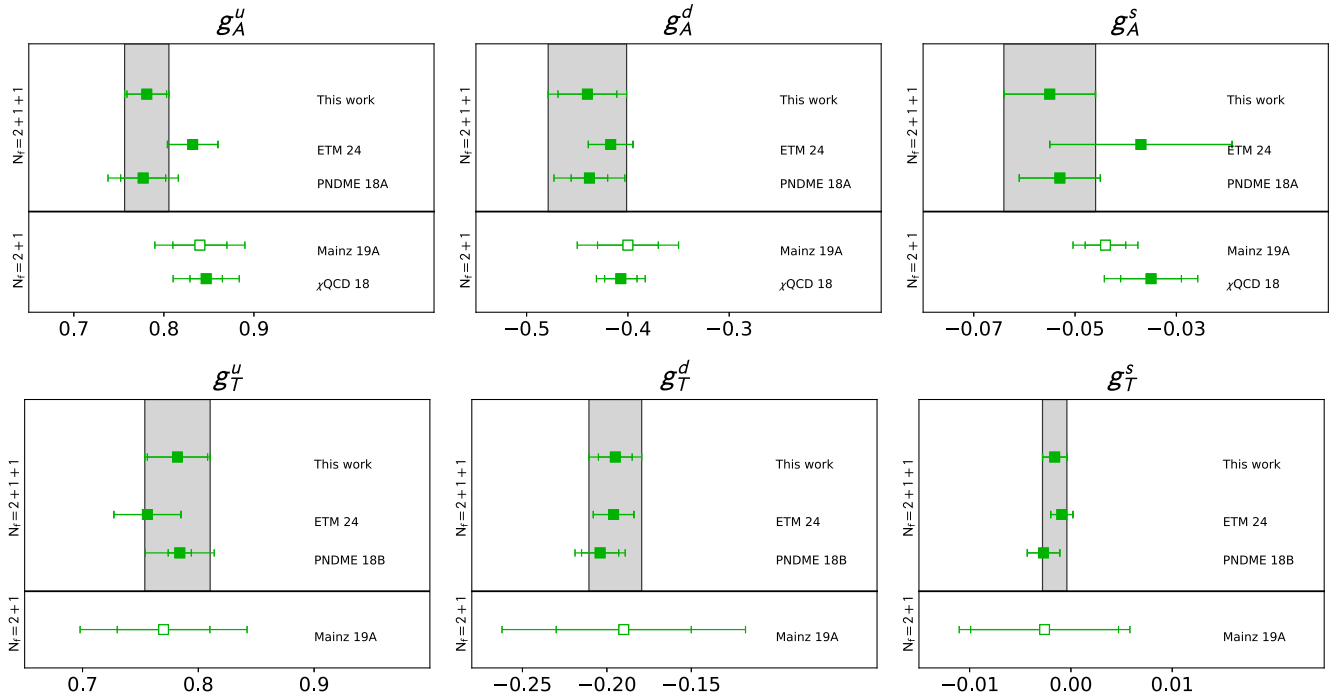


FIG. 6. Comparison of axial and tensor charges for the proton with other lattice calculations using $2+1+1$ and $2+1$-flavors of quarks that meet the FLAG criteria. Results for the neutron are given by the $u \leftrightarrow d$ interchange. Unfilled symbols indicate that these results have not yet been published or are conference proceedings. The references are ETM 24 [39], PNDME 18A [3], PNDME 18B [4], Mainz 19A [40], and χQCD 18 [41].

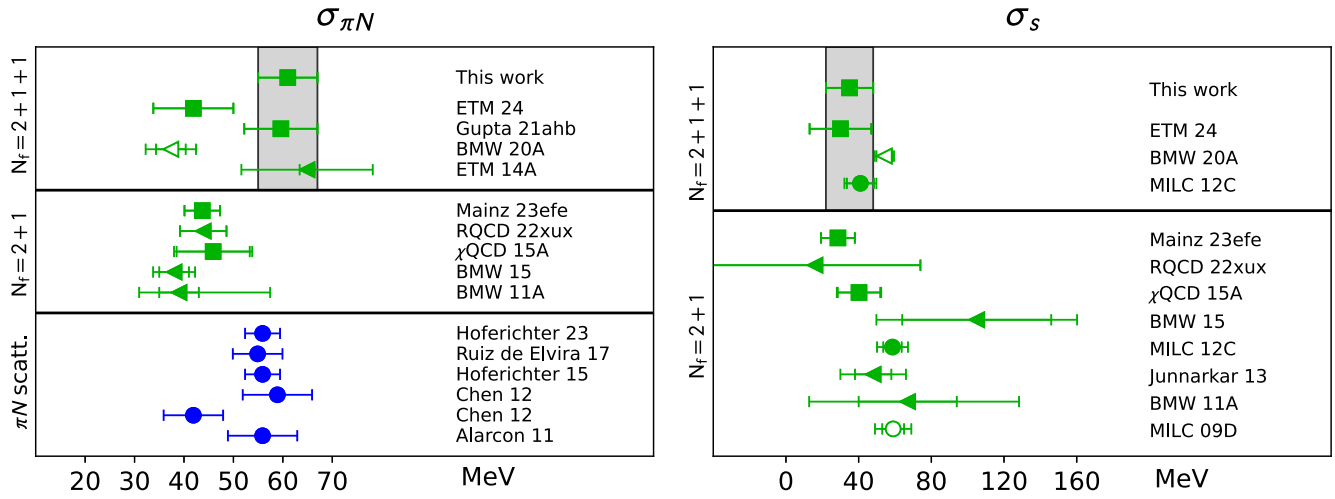


FIG. 7. Left: results for $\sigma_{\pi N} = m_{ud} g_S^{u+d}$ from $2+1$- and $2+1+1$-flavor lattice calculations that satisfy the FLAG criteria for inclusion in averages. The BMW 20 $1+1+1+1$-flavor result is still a preprint and listed here under $2+1+1$-flavor calculations for brevity. We follow the FLAG conventions and denote direct determinations by squares and the results obtained using the Feynman-Hellmann method by triangles. The references for the lattice results are: ETM 24 [39], Gupta 21ahb [5], BMW 20A [42] ETM 14A [43], Mainz 23ehe [44] RQCD 22xux [45] χQCD 15A [46], BMW 15 [47], BMW 11A [42]. The phenomenological estimates (blue filled circles), obtained using πN scattering data, are from Hoferichter 23 [48], Ruiz de Elvira 17 [49], Hoferichter 15 [50], Chen 12 [51], and Alarcon 11 [52]. Right: results for σ_s. The additional references for σ_s are MILC 12C [53], Junnarkar 13 [54], and MILC 09D [55].

scattering experiments at Jefferson Lab and other facilities worldwide [58–60]. These charges also give the intrinsic contributions of the electric dipole moments of the quarks to the neutron/proton EDM [4].

Our results for the scalar charges, $g_S^{u,d,s}$, are new with only preliminary versions presented in conference proceedings [7,8]. Most of the discussion of scalar charges in literature has been in terms of the sigma terms, the pion-nucleon, $\sigma_{\pi N}$, and the strangeness content σ_s [61]. For the pion-nucleon sigma term $\sigma_{\pi N}$, the main issue, first raised in Ref. [5], is removing the contributions of multihadron $N\pi$ and $N\pi\pi$ states that are lattice artifacts. Our selection of the $N\pi$ analysis results, as discussed in Sec. VI D, rely on the χPT analysis and the phenomenological observation of a large scalar condensate in QCD. Results in Eq. (10) are consistent with those presented in Ref. [5]. The value $\sigma_s = 35(13)$ MeV reflects the large uncertainty in the calculation of g_S^s and the CCFV extrapolation as shown in Fig. 16. A comparison with other lattice and phenomenological results in the FLAG format is shown in Fig. 7. Our result $\sigma_{\pi N}|_{\text{standard}} = 42(6)$ MeV is consistent with other lattice measurements, while our preferred value $\sigma_{\pi N}|_{N\pi} = 61(6)$ MeV is in agreement with phenomenological extraction (dispersive analysis of πN scattering data).

Note that a larger value of the scalar charges, output of our $N\pi$ analyses motivated by χPT, has a significant impact on the reach of dark matter direct-detection experiments—a $\approx$50% larger $g_S^{u,d}$ increases the cross section by a factor of $\approx$2.25 assuming the couplings to dark matter are in the most promising scalar channel. In fact, all three sets of charges, $g_{A,S,T}^{u,d,s}$, give the coupling of dark matter or novel Higgs-like interactions to nucleons in the respective Lorentz channels.

The most direct comparison of our results is with the latest results from the ETM Collaboration 24 [39], who have analyzed three physical mass ensembles using $2+1+1$-flavors of twisted mass fermions. We note that these new ETM results supersede all their previously published values as explained in Ref. [39].

The two sets of results, summarized in Figs. 6 and 7, are consistent with two notable (2σ) differences: in $g_A^{l,s}$ and $\sigma_{\pi N}$. The reasons are:

(i) Our data show ESCs in $g_A^{l,s}$ (see Figs. 2 and 3) while the ETM data (labeled $g_A^{u+d(\text{disc})}$ and $g_A^{s(\text{disc})}$) are flat even though they include data at smaller τ, i.e., in the range $0.41 < \tau < 1.6$ fm versus $0.9 < \tau < 1.5$ fm in our calculation. This accounts for most of the difference in the final values of $g_A^{u,d}$ shown in Fig. 6.

(ii) Both calculations find large ESCs in $g_S^{u,d,s}$. The difference in the estimates of $\sigma_{\pi N}$ comes from the choice of ESC fits. We have chosen the $N\pi$ fit for the final answer based on our χPT analysis [5]. Had we chosen our standard analysis value, as ETM does, the two results would be consistent.

In summary, as already remarked in Sec. V, the largest uncertainty in these two quantities in our work comes from the ESC fits and possible contributions from $N\pi$ states. The ETM results are from a standard analysis.

Looking ahead, we are analyzing two physical pion mass HISQ ensembles at $a \approx 0.087$ and 0.057 fm with about six times larger statistics (6000 and 4000 configurations,

respectively) and better tuned values of m_s and m_l in the clover action. These calculations will improve control over excited-state analysis and, hopefully, the statistics are large enough to provide a data driven resolution between the standard and $N\pi$ analyses.

The calculations in this paper used the Chroma software suite [26].

ACKNOWLEDGMENTS

We thank the MILC Collaboration for providing the $2+1+1$-flavor HISQ lattices, and acknowledge John Gracey for discussions on the renormalization of the currents. This research used resources at (i) the National Energy Research Scientific Computing Center, a DOE Office of Science User Facility supported by the Office of Science of the U.S. Department of Energy under Contract No. DE-AC02-05CH11231; (ii) the Oak Ridge Leadership Computing Facility, which is a DOE Office of Science User Facility supported under Contract DE-AC05-00OR22725, through the ALCC program project LGT107 and HEP145, and the INCITE program project HEP133; (iii) the USQCD collaboration, which is funded by the Office of Science of the U.S. Department of Energy; and (iv) Institutional Computing at Los Alamos National Laboratory. This work was prepared in part by LLNL under Contract No. DE-AC52-07NA27344. S. P. acknowledges support from the ASC COSMON project. S. P. acknowledges support from the U.S. DOE Contract No. DE-AC05-06OR23177, under which Jefferson Science Associates, LLC, manages and operates Jefferson Lab. Also acknowledged is support from the Exascale Computing Project (17-SC-20-SC), a collaborative effort of the U.S. DOE Office of Science and the National Nuclear Security Administration. T. B. and R. G. were partly supported by the U.S. Department of Energy, Office of Science, Office of High Energy Physics under Contract No. DE-AC52-06NA25396. T. B., R. G., S. M., S. P., and B. Y. were partly supported by the LANL LDRD program, and S. P. by the Center for Nonlinear Studies.

DATA AVAILABILITY

The data that support the findings of this article are available to all researchers upon reasonable requests to the corresponding author.

APPENDIX A: CHIRAL-CONTINUUM-FINITE-VOLUME EXTRAPOLATION FOR $g^{u,d,s}_{A,S,T}$

Figures 8–16 in this appendix show the CCFV fits used to extrapolate the data for the charges on the eight

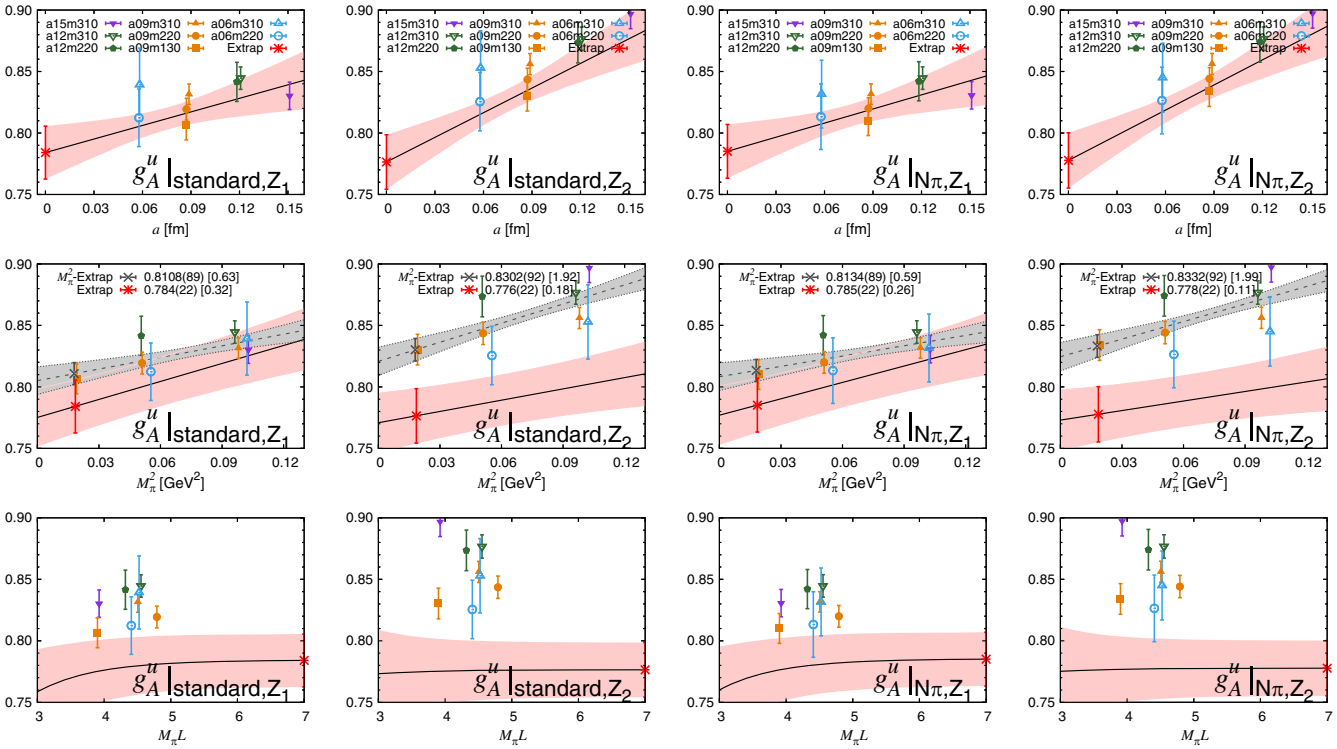


FIG. 8. CCFV extrapolation for g_A^u using Eq. (7). The three panels in each column show the result of the simultaneous fit (pink bands) plotted versus a, M_π^2 and $M_\pi L$, respectively, with the other two variables set to their physical point values. The gray band shows a chiral fit, i.e., assuming $c_1 = c_3 = 0$ in Eq. (7). Each row shows, from left to right, the fits for the four different analyses: (i) $\{\text{standard}, Z_1\}$, (ii) $\{\text{standard}, Z_2\}$, (iii) $\{N\pi, Z_1\}$ and (iv) $\{N\pi, Z_2\}$. The red star is the value at the physical point given by the CCFV fit and the black cross is the result of just the chiral fit. The numbers within square parentheses in the middle panels are the χ^2/dof of these fits.

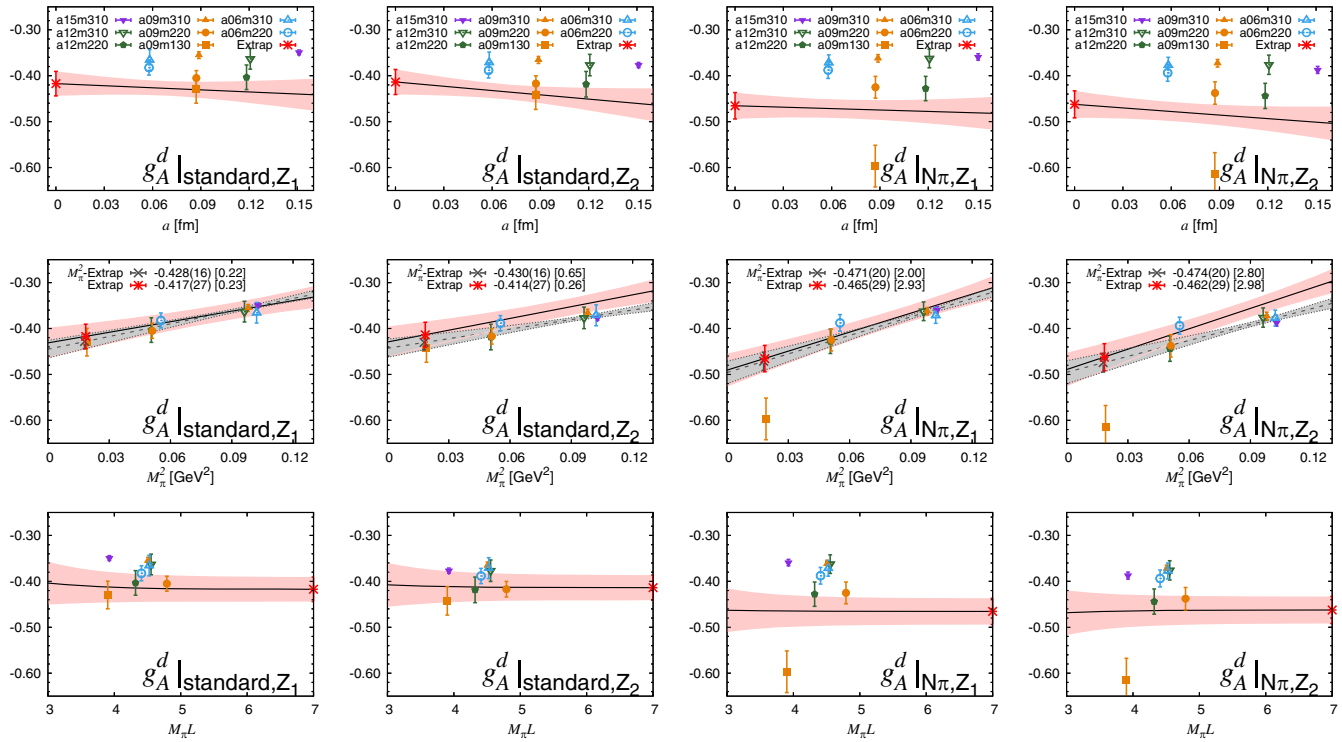


FIG. 9. CCFV extrapolation for g_A^d using Eq. (7). The rest is the same as in Fig. 8.

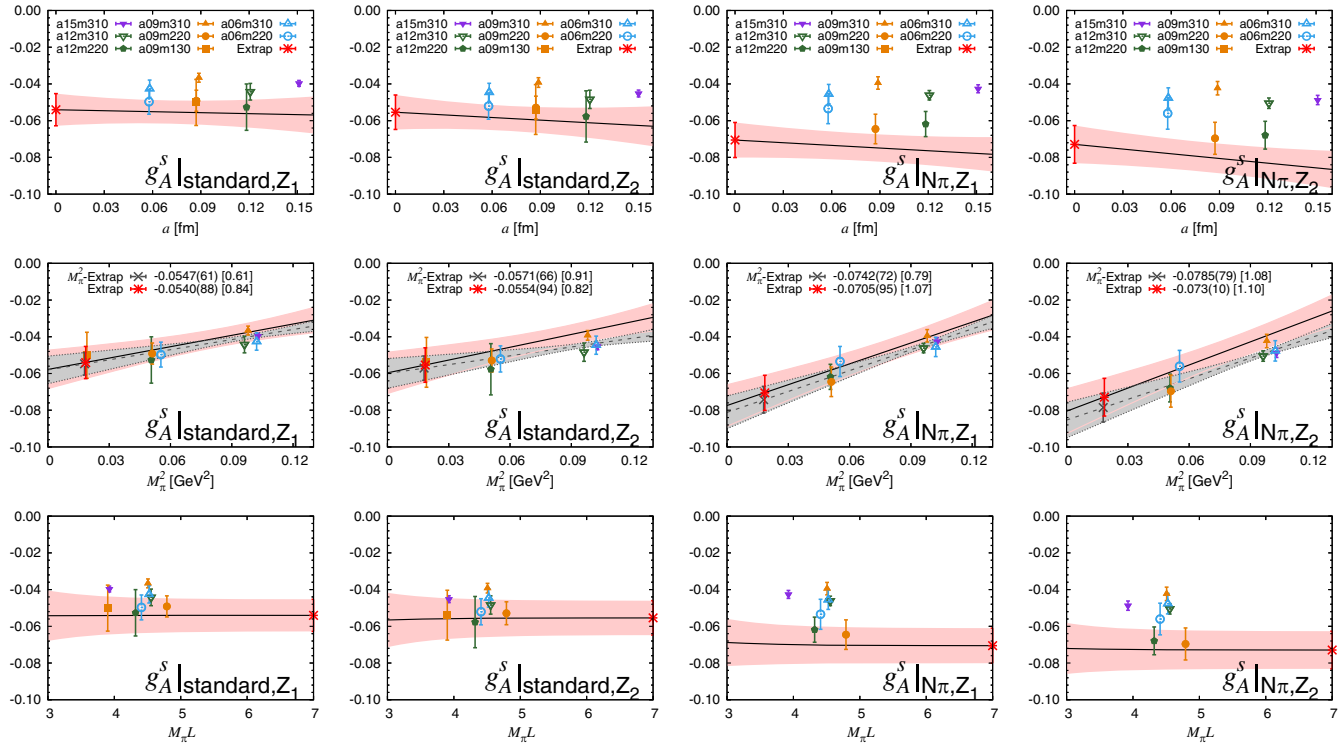


FIG. 10. CCFV extrapolation for g_A^s using Eq. (7). The rest is the same as in Fig. 8.

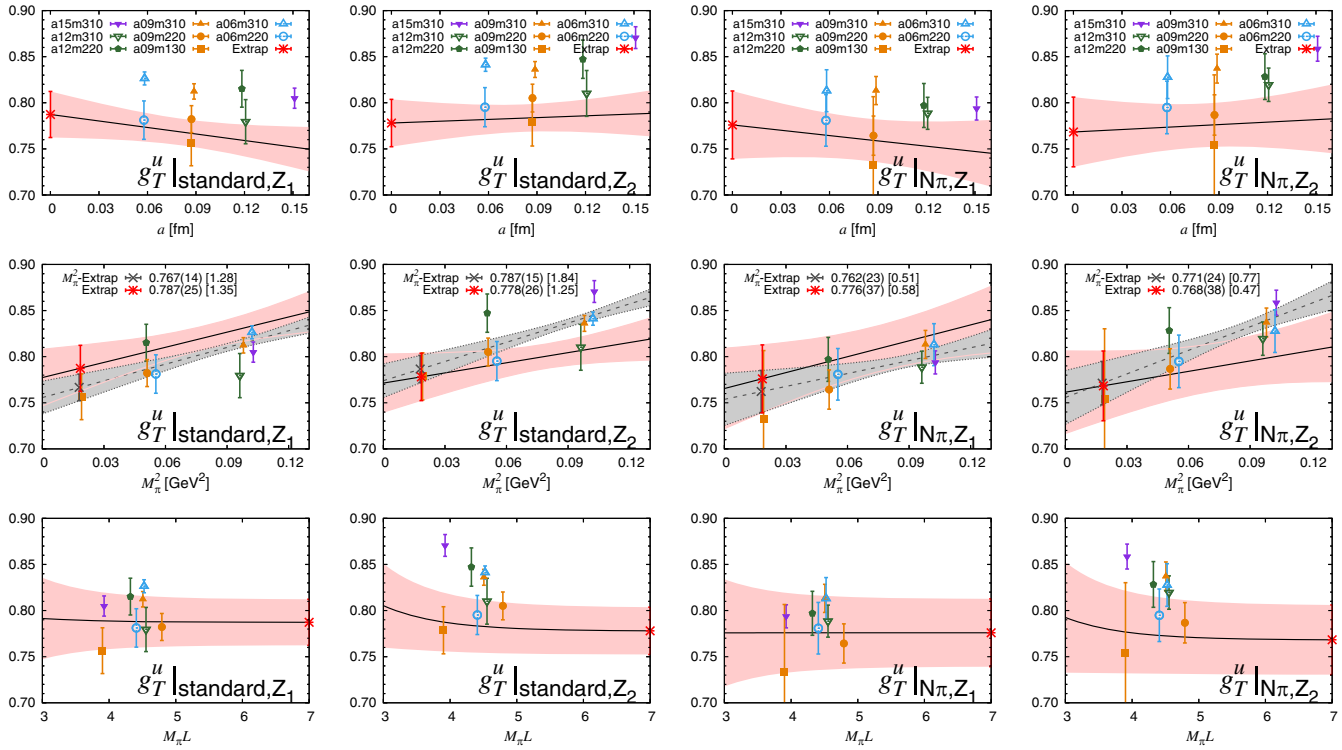


FIG. 11. CCFV extrapolation for g_T^u using Eq. (7). The rest is the same as in Fig. 8.

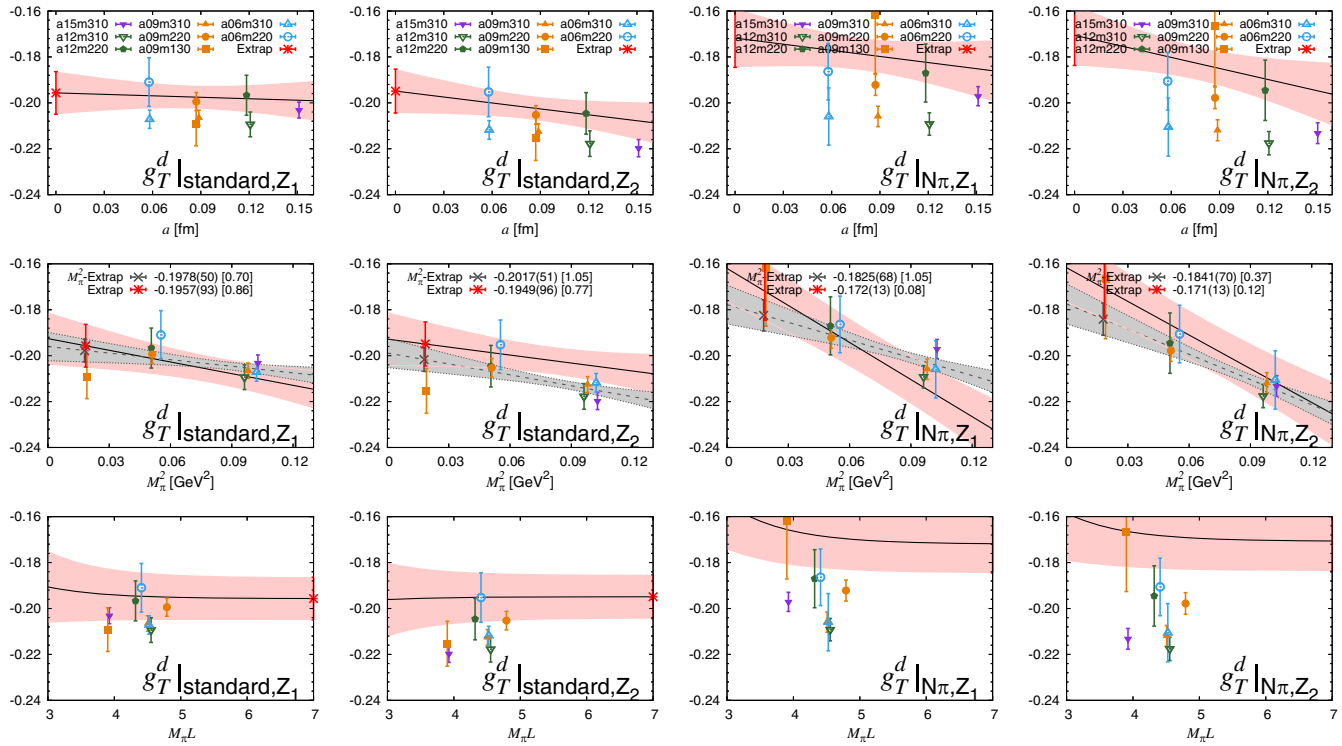


FIG. 12. CCFV extrapolation for g_T^d using Eq. (7). The rest is the same as in Fig. 8.

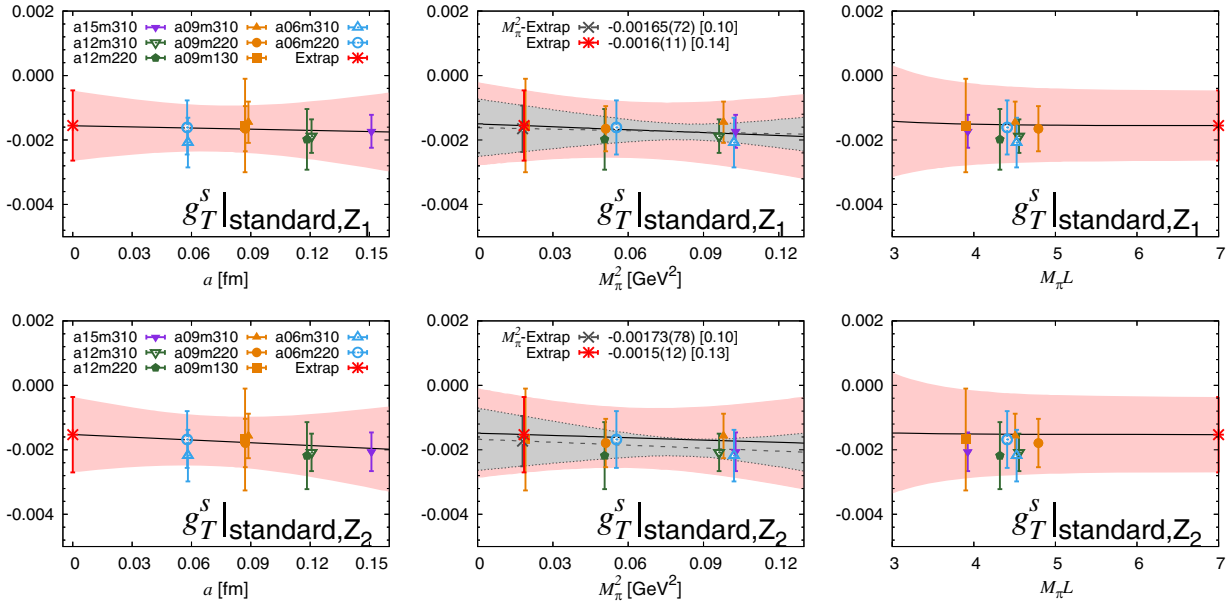


FIG. 13. CCFV extrapolation for g_T^s using Eq. (7). The rest is the same as in Fig. 8. These data are only analyzed using the standard strategy as the likely multihadron lowest excited state, ΣK, is heavier than the $N(1440)$ radial excitation.

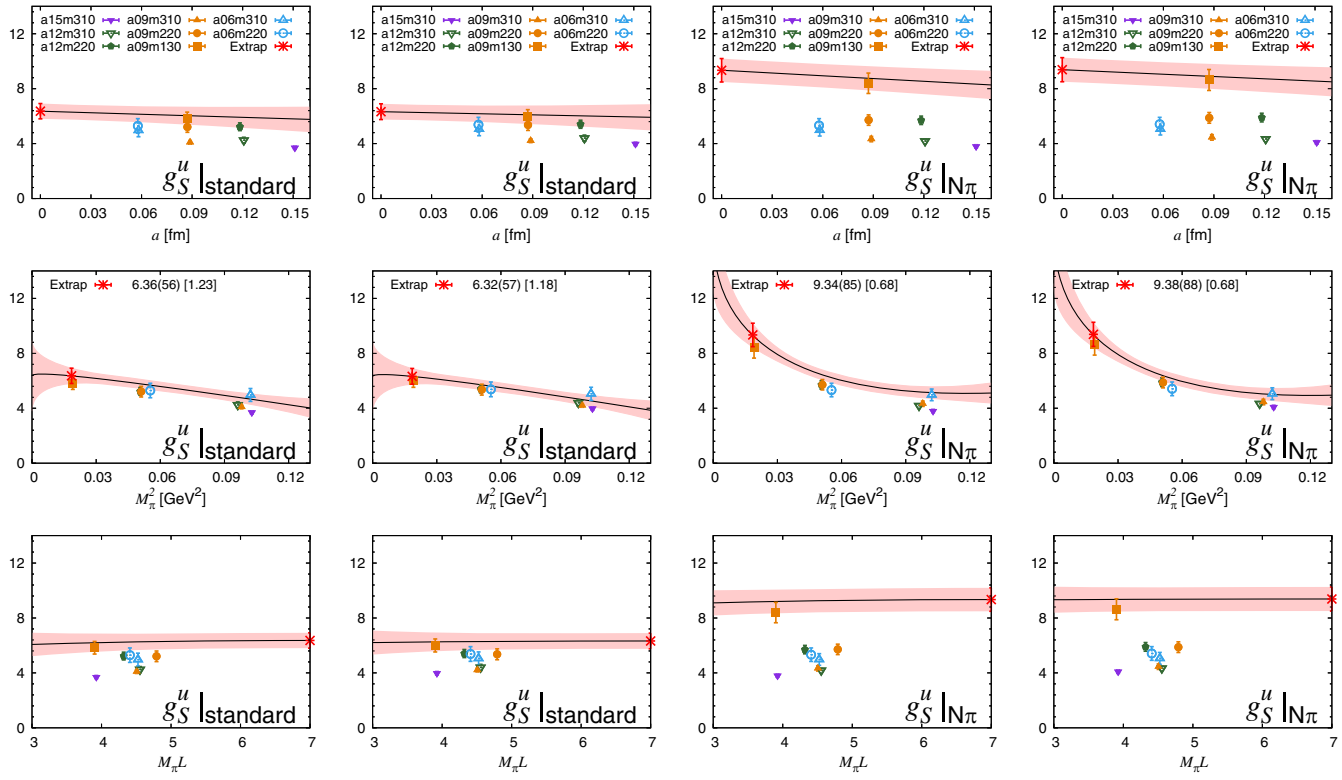


FIG. 14. CCFV extrapolation for g_S^u using Eq. (8). The rest is the same as in Fig. 8.

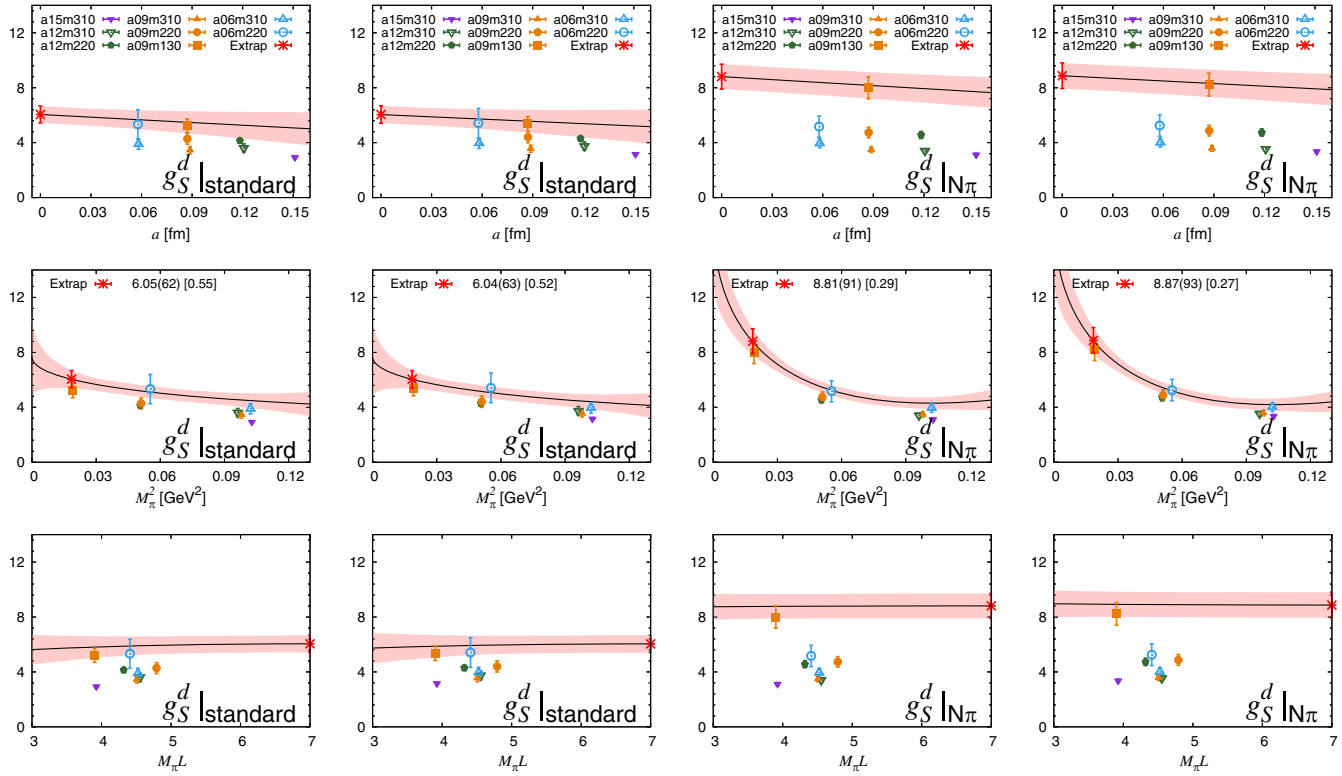


FIG. 15. CCFV extrapolation for g_S^d using Eq. (8). The rest is the same as in Fig. 8.

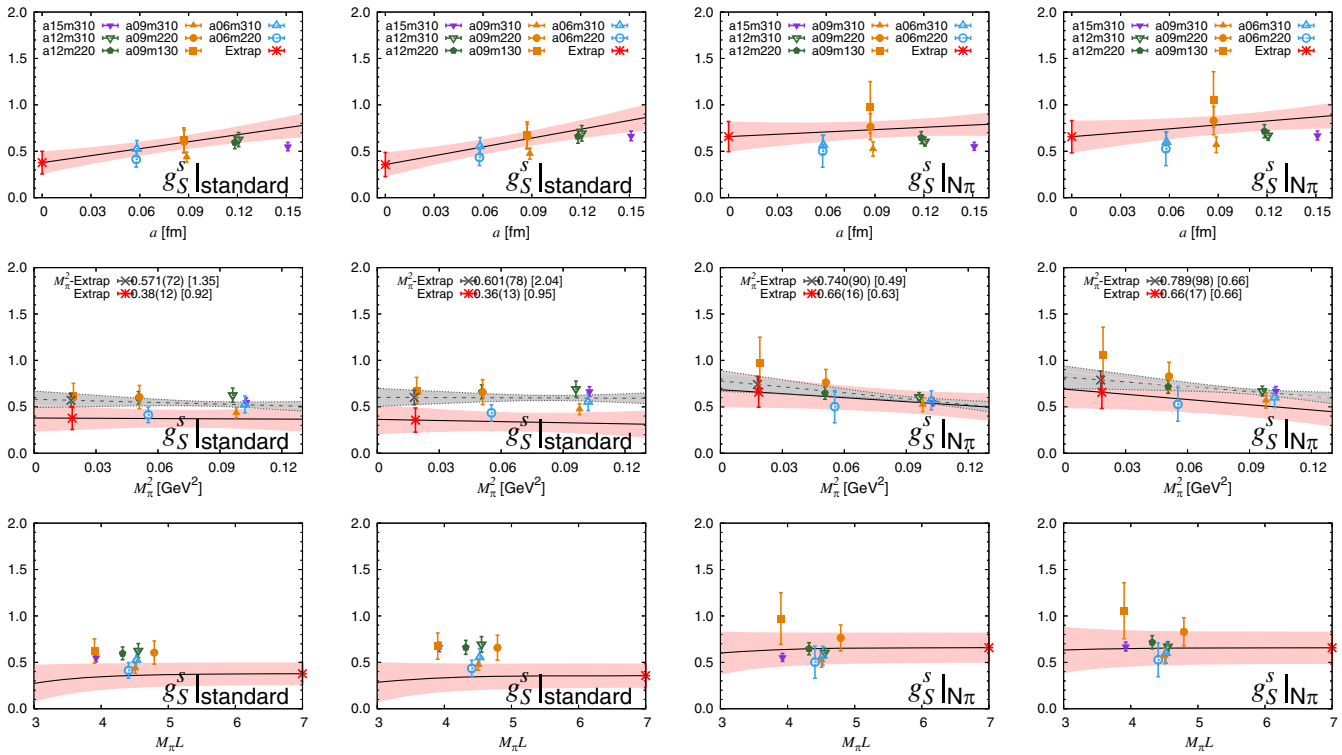


FIG. 16. CCFV extrapolation for g_S^s. The rest is the same as in Fig. 8.

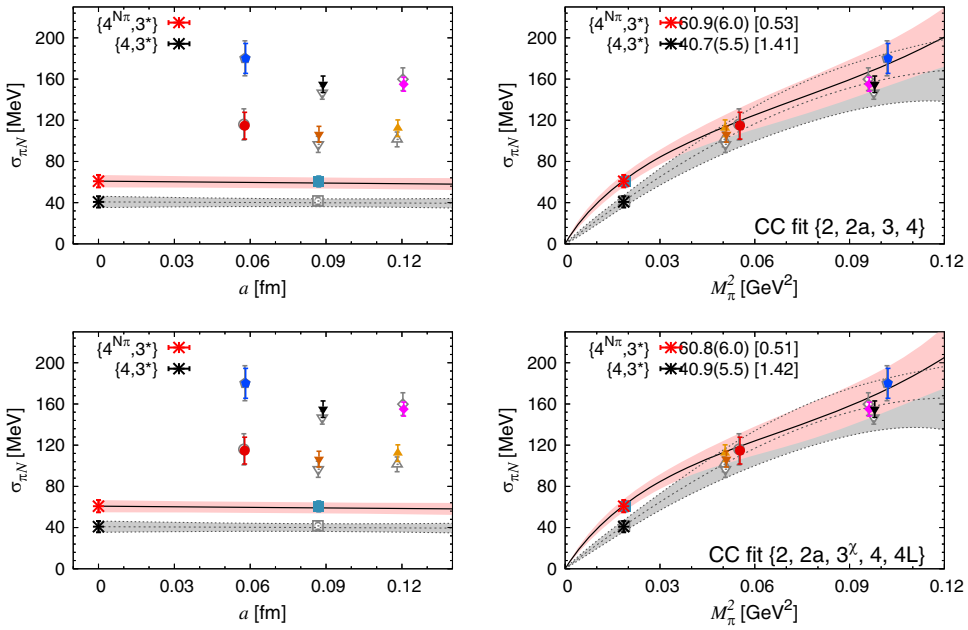


FIG. 17. The chiral-continuum extrapolation for $\sigma_{\pi N} = m_{ud} g_S^{u+d}$ using the *Ansatz* given in Eq. (9). In the bottom fit, the logarithm term in Eq. (9) is included by setting the coefficient d_3^χ to its χPT value taken from Ref. [5]. Both fits, therefore, have four free parameters. The color (gray/black) bands and points correspond to the $N\pi$ (standard) analysis.

ensembles to the physical point. In each column, the three panels show the simultaneous CCFV fit (pink band) plotted versus either a or M_π^2 or $M_\pi L$, respectively, with the other two variables set to their physical point values. In the panels plotted versus M_π^2, the additional gray bands show the fit with only the chiral corrections included in Eqs. (7) or (8). Note that when the discretization and finite volume corrections are small, the gray bands overlap with the CCFV fits (pink bands). The results of these fits are summarized in Table VI.

APPENDIX B: NONPERTURBATIVE RENORMALIZATION FOR THE 2 + 1-FLAVOR THEORY USING THE RI-sMOM SCHEME

This appendix presents an overview of the calculation of the renormalization constants for the flavor diagonal quark bilinear operators $\mathcal{O}^f = \bar{\psi}^f \Gamma \psi^f$ with Dirac matrix Γ and the flavor index $f = \{u, d, s\}$ in the $N_f = 3$ theory. The lattice calculation is done in the RI-sMOM scheme [9,10] on four ensembles at the different values of the lattice spacing used in this study: $a15m310$, $a12m310$, $a09m310$, and $a06m310$. Since data are obtained at only one value of $M_\pi \neq 0$ at each a, we explicitly assume that the quark mass dependence can be neglected and these results are a good approximation to the chiral limit values. Second, the lattice calculation is not fully $O(a)$ improved in neither the action nor the operators. In the latter, we neglect all the lattice spacing dependent improvement terms. Consequently, the results for the renormalized charges are extrapolated to the continuum limit using an *Ansatz* starting with a term linear in a.

Results for the matching factors between the RI-sMOM and the $\overline{\text{MS}}$ scheme, and the running in the $\overline{\text{MS}}$ scheme are taken from continuum perturbation theory [62–67] as specified in Appendix B 3.

The general relation between renormalized, $\mathcal{O}_R$, and bare, $\mathcal{O}$, operators including mixing between flavors is

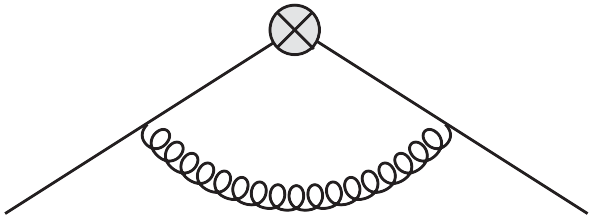
$$\mathcal{O}_R^f = \sum_{f'} Z_\Gamma^{ff'} \mathcal{O}^{f'}, \tag{B1}$$

with the matrix $Z_\Gamma^{ff'}$ determined nonperturbatively on the lattice using the regularization independent (RI) renormalization scheme [9] in which the renormalized vertex function is set to its tree-level value. The calculation is done with the gauge fields fixed to the Landau gauge and quark propagators generated using momentum sources. The final results for the three charges, using the two methods, labeled Z_1 and Z_2 and discussed in Appendix B 4, for partially removing discretization errors are given in Appendix B 5.

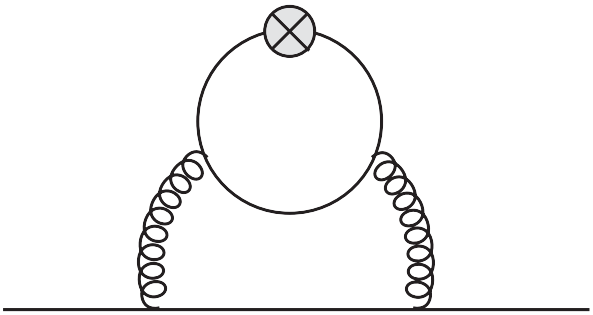
1. Flavor mixing in the RI scheme

The calculation starts with the amputated vertex function $\Gamma^{ff'}(p_1, p_2)$ defined as

$$\Gamma^{ff'}(p_1, p_2) = \langle S^f(p_1)\rangle^{-1} \langle \psi^f(p_1) \mathcal{O}^{f'} \psi^f(p_2)\rangle \langle S^f(p_2)\rangle^{-1}, \tag{B2}$$



(a) The connected vertex $\Gamma_{\rm conn}(m,\mu^2)$



(b) The disconnected vertex $\Gamma_{\rm disc}(m_f,m_{f'},\mu^2)$

FIG. 18. Amputated vertex diagrams defined in Eq. (B2).

where ψ^f and S^f are the quark field and propagator with flavor-f. The three-point function $\langle\psi^f(p_1)\mathcal{O}^{f'}\psi^f(p_2)\rangle$ gets contributions from both the connected and the disconnected diagrams shown in Fig. 18. The perturbative result for this Green's function $\Gamma^{ff'}(p_1,p_2)$ in the $\overline{\rm MS}$ scheme is given in Refs. [64,68] in terms of its Lorentz's components.

Next, we define the projection operators $\mathbb{P}_\Gamma$ used in this calculation to be $\mathbb{1}/4, \not{q}q^\mu/4q^2, \gamma_5\not{q}q^\mu/4q^2, i\gamma^{[\mu}\gamma^{\nu]}/48$ for the scalar, vector, axial and tensor operators [19]. The normalization $\mathrm{Tr}[\gamma_\mu\gamma_\nu]=\delta_{\mu\nu}\mathbb{1}$ is implied. Then, in the RI-sMOM scheme, the projected renormalized amputated vertex function is fixed to its tree-level value, as follows:

$$\mathrm{Tr}[\mathbb{P}_\Gamma\Gamma_R^{ff'}(p_1,p_2)]\equiv\frac{Z_\Gamma^{f'f''}}{Z_\psi^f}\mathrm{Tr}[\mathbb{P}_\Gamma\Gamma^{ff''}(p_1,p_2)]=\delta^{ff'}. \tag{B3}$$

This relation defines the 3×3 mixing matrix Z_Γ for the three-flavor theory in the RI-sMOM scheme, as follows:

$$Z_\Gamma=\left[\frac{1}{Z_\psi^f}\mathrm{Tr}\big(\mathbb{P}_\Gamma\Gamma(p_1,p_2)^T\big)\right]^{-1}. \tag{B4}$$

The determination of Z_ψ^f is done in a separate calculation using two different methods as discussed in Sec. B 4.

The amputated vertex function $\Gamma^{ff'}$ gets contributions from both the connected and disconnected diagrams shown in Fig. 18, as follows:

$$\Gamma^{ff'}(p_1,p_2)=\Gamma_{\rm conn}(m^f,\mu^2)\delta^{ff'}-\Gamma_{\rm disc}(m^f,m^{f'},\mu^2). \tag{B5}$$

The $(-)$ sign in $\Gamma_{\rm disc}$ is due to the anticommuting nature of the fermion fields contracted into the quark loop. On the lattice we calculate the projected amputated vertex functions c_f (connected) and $d_{ff'}$ (disconnected) defined as

$$c_\Gamma^f=\frac{1}{Z_\psi^f}\mathrm{Tr}[\mathbb{P}_\Gamma\Gamma_{\rm conn}(m^f,\mu^2)] \tag{B6}$$

$$d_\Gamma^{ff'}=\frac{1}{Z_\psi^f}\mathrm{Tr}[\mathbb{P}_\Gamma\Gamma_{\rm disc}(m_f,m_{f'},\mu^2)]. \tag{B7}$$

For the $N_f=2+1$ isospin symmetric theory relevant to this work, the determination of $Z_\Gamma^{ff'}$ requires calculating the following six quantities on the lattice,

$$c_\Gamma^l, c_\Gamma^s, d_\Gamma^{ll}, d_\Gamma^{ls}, d_\Gamma^{sl}, \text{ and } d_\Gamma^{ss}, \tag{B8}$$

for each Γ. Working in the flavor basis $f\in\{u-d,u+d,s\}$, the Z_Γ, defined in Eq. (B4), is block diagonal, as follows:

$$Z_\Gamma\equiv\begin{pmatrix}Z_\Gamma^{u-d,u-d}&0&0\\0&Z_\Gamma^{u+d,u+d}&Z_\Gamma^{u+d,s}\\0&Z_\Gamma^{s,u+d}&Z_\Gamma^{ss}\end{pmatrix} \tag{B9}$$

$$=\begin{pmatrix}c_\Gamma^l&0&0\\0&c_\Gamma^l-2d_\Gamma^{ll}&-2d_\Gamma^{sl}\\0&-d_\Gamma^{ls}&c_\Gamma^s-d_\Gamma^{ss}\end{pmatrix}^{-1}. \tag{B10}$$

For the discussion of the matching and running, the more convenient basis is the isovector (3), octet (8), and singlet (0) one, i.e., $f\in\{u-d,u+d-2s,u+d+s\}$. In this case the renormalization matrix in terms of the six quantities is

$$\begin{pmatrix}Z_\Gamma^{3,3}&0&0\\0&Z_\Gamma^{8,8}&Z_\Gamma^{8,0}\\0&Z_\Gamma^{0,8}&Z_\Gamma^{0,0}\end{pmatrix}=\begin{pmatrix}c_\Gamma^l&0&0\\0&\frac{1}{3}\left(c_\Gamma^l+2(c_\Gamma^s-d_\Gamma^{ll}+d_\Gamma^{ls}+d_\Gamma^{sl}-d_\Gamma^{ss})\right)&\frac{2}{3}\left(c_\Gamma^l-c_\Gamma^s-2d_\Gamma^{ll}+2d_\Gamma^{ls}-d_\Gamma^{sl}+d_\Gamma^{ss}\right)\\0&\frac{1}{3}\left(c_\Gamma^l-c_\Gamma^s-2d_\Gamma^{ll}-d_\Gamma^{ls}+2d_\Gamma^{sl}+d_\Gamma^{ss}\right)&\frac{1}{3}\left(2c_\Gamma^l+c_\Gamma^s-4d_\Gamma^{ll}-2d_\Gamma^{ls}-2d_\Gamma^{sl}-d_\Gamma^{ss}\right)\end{pmatrix}^{-1}. \tag{B11}$$

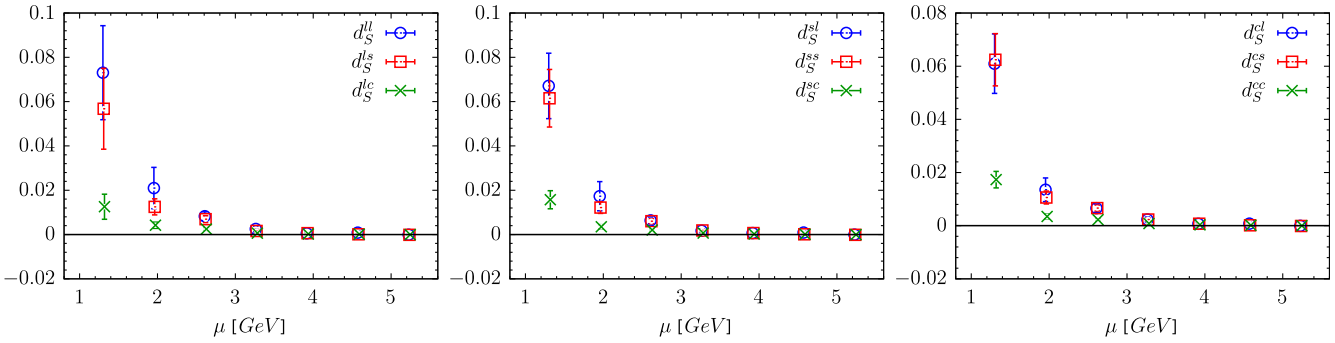


FIG. 19. Data for the disconnected projected amputated Green's function $d_\Gamma^{ff'}$ for a quark with flavor $f \in \{l, s, c\}$ and the disconnected loop with flavor f' for the scalar bilinear operator $O_S^{f'}$ in the RI-sMOM scheme. The allowed momenta satisfy $\mu^2 = p^2 = p'^2 = (p - p')^2$. Data for the charm quark are also plotted to show the dependence on the quark mass even though they are not used in this work.

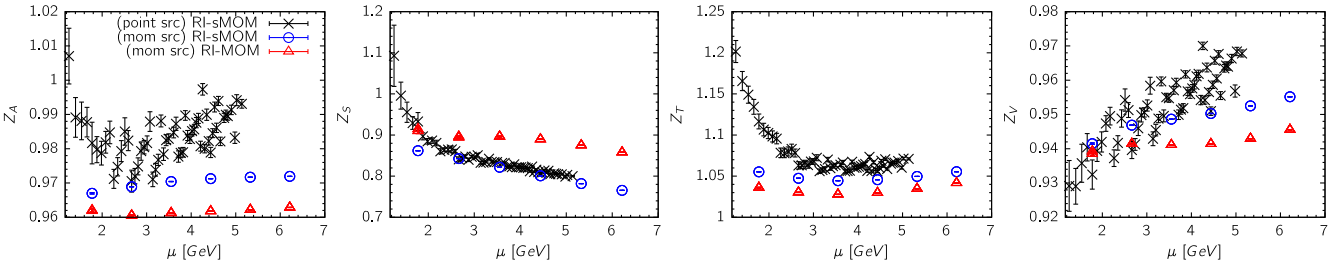


FIG. 20. These plots show the improvement in the calculation of the four renormalization factors in the RI-sMOM scheme obtained using momentum (mom src) versus point source propagators (point src). The data are for the a06m310 ensemble. For comparison, we also show the factors obtained in the RI-MOM scheme even though they are not used in this work.

2. RI-sMOM scheme

The lattice calculation is done in the RI-sMOM scheme [10] where the four-momentum of the external legs $\{p_1, p_2\}$ satisfies the symmetric momentum condition $p_1^2 = p_2^2 = (p_1 - p_2)^2 = \mu^2$, and μ^2 defines the renormalization scale. We find that the matrix $Z^{\text{RI-sMOM}}(\mu)$ is close to diagonal with $c_\Gamma^l \sim O(1)$ and $d_\Gamma^{ff'}$ about a few percent at $\mu \sim 2$ GeV. This is illustrated in Fig. 19 for the scalar operator (largest mixing) for three of the disconnected projected amputated Green's functions d_Γ^{lf} calculated at various μ. As expected, the value decreases as the quark mass in the loop is increased from light to strange to charm. To get a signal for this small mixing, we use momentum source propagators [69] in Landau gauge and take the momenta $\{p_1, p_2\}$ to be proportional to (1, 1, 1, 1) to minimize $O(4)$-symmetry breaking. A comparison of the improvement in the extraction of Z using momentum versus point sources is shown in Fig 20.

3. Matching and RG running

The calculation of the renormalization factors for each operator involves the four steps described below.

(1) To obtain the full 3×3 matrix, $Z^{\text{RI-sMOM,latt}}(\mu)$ defined in Eq. (B10), the two c_f and four $d_{ff'}$ (Fig. 19) are calculated using momentum source propagators with the lattice fixed to Landau gauge. The simulations are done for a range of lattice momenta satisfying $q^2 = p_1^2 = p_2^2 \equiv \mu_{\text{latt}}^2$.

(2) For each μ_{latt}, a horizontal matching, $\mu_{\text{cont}} = \mu_{\text{latt}}$, to $\overline{\text{MS}}$ scheme is performed by multiplying $Z^{\text{RI-sMOM,latt}}(\mu)$ with the matching factor $C^{\text{RI-sMOM}\to\overline{\text{MS}}}(\mu)$ calculated using perturbation theory in the continuum:

$$Z^{\overline{\text{MS}}}(\mu) = C^{\text{RI-sMOM}\to\overline{\text{MS}}}(\mu) Z^{\text{RI-sMOM,latt}}(\mu). \quad \text{(B12)}$$

(3) The result for each μ is run in the continuum to a common scale, which we choose to be 2 GeV:

$$Z^{\overline{\text{MS}}}(2\ \text{GeV}; \mu) = C^{\overline{\text{MS}}}(2\ \text{GeV}, \mu) Z^{\overline{\text{MS}}}(\mu). \quad \text{(B13)}$$

(4) Lattice artifacts giving rise to a μ dependence. These are removed using the *Ansatz*

$$Z^{\overline{\text{MS}}}(2\ \text{GeV}; \mu) = Z^{\overline{\text{MS}}}(2\ \text{GeV}) + c_1 \mu^2 + c_2 \mu^4. \quad \text{(B14)}$$

Note that, in the RI-sMOM calculation, there are, in general, not enough data points at small μ^2 to include

$1/\mu^2$ term as was done in Refs. [19,70]. We, therefore, fit to points with $\mu^2_{\rm min}$ large enough so that the contribution of a $1/\mu^2$ term can be assumed to be negligible.

The final results for $Z^{\overline{\rm MS}}_{\{A,S,T\}}(2\ {\rm GeV})$ are given in Appendix B 5. We remind the reader of the implicit assumption that the possible quark mass dependence has been neglected and the results obtained at $M_\pi \neq 0$ are a good approximation to the chiral limit values.

In the continuum calculation of $C^{\rm RI-sMOM\to\overline{MS}}(\mu)$ and $C^{\overline{\rm MS}}(2\ {\rm GeV},\mu)$ for the scalar, tensor and pseudoscalar operators, the singlet and nonsinglet factors are the same because the disconnected loops vanish in the zero mass limit due to chirality. Thus the 3×3 matrices for the matching and running reduce to an overall factor, for example, $C^{\rm RI-sMOM\to\overline{MS}}(\mu) = Z^{\rm match}\times \mathbb{1}$. The three-loop result for the scalar and tensor can be obtained, after projection, from the amputated Green's functions given in Ref. [62]:

$$\begin{aligned} Z^{\rm match}_{S,{\rm SMOM}} &= 1 + 0.64552a + (23.024 - 4.0135n_f)a^2 \\ &\quad + (2.1844n_f^2 - 169.923n_f + 889.74)a^3, \\ Z^{\rm match}_{T,{\rm SMOM}} &= 1 - 0.215a + (4.103n_f - 43.384)a^2 \\ &\quad - (7.0636n_f^2 - 309.828n_f + 1950.76)a^3, \end{aligned} \tag{B15}$$

where $a(\mu)\equiv\alpha_s(\mu)/4\pi$. The running factor, $C^{\overline{\rm MS}}(2{\rm GeV},\mu)$ for the tensor is obtained from the four-loop results in Ref. [64], and for the scalar the five-loop result in Ref. [63].

The matching and running factors are unity for both the singlet and nonsinglet vector operator because of the conservation of the vector current. The renormalization factor Z_V for the bare local operator is given by the relation $Z_V g_V = 1$, with g_V obtained from the forward matrix element as discussed in Appendix B 4.

For the axial operator, only the flavor nonsinglet axial current is conserved in the chiral limit. Therefore the matching from RI-sMOM to $\overline{\rm MS}$ scheme and the renormalization group (RG) running factor is unity for the nonsinglet operator.

The flavor singlet axial current is not conserved due to the $U_A(1)$ anomaly, and the renormalization factors become nontrivial at the two-loop level. This $1+\mathcal{O}(\alpha^2)$ correction is taken from Refs. [68,71], and the three-loop anomalous dimension from Ref. [72] is used for the RG running.[2]

[2]The four-loop anomalous dimension for the isosinglet axial current in the continuum in the $\overline{\rm MS}$ scheme has been calculated in Ref. [73]. We use the three-loop running for consistency with the RI-sMOM to $\overline{\rm MS}$ matching that has been calculated to only two loops.

The off-diagonal terms in the mixing matrix for the singlet axial current are zero in the chiral limit, leaving only the diagonal elements. The difference between the singlet and nonsinglet (the disconnected contribution) has been calculated in the $\overline{\rm MS}$ scheme in the RI-sMOM setup in Ref. [68]. This is used to get the following matching factor for the axial current in the $\{3,8,0\}$ basis:

$$C_A^{\rm RI-sMOM\to\overline{MS}}(\mu) = \begin{pmatrix} 1 & 0 & 0 \\ 0 & 1 & 0 \\ 0 & 0 & 1 - 26.5a^2 n_f \end{pmatrix}. \tag{B16}$$

In the calculation of all the matching and running factors, the number of flavors used is $n_f = 4$. We have checked that the difference in the final results between using $n_f = 3$ and 4 is below the claimed precision.

On the lattice, Wilson-clover fermions break chiral symmetry explicitly and there are nonzero contributions from disconnected loops for all charges. These give rise to off-diagonal terms as shown in Eqs. (B10) and (B11). The mixing in the tensor channel is $O(\alpha_s^3)$ in lattice perturbation theory [74] implying $r_T \equiv Z_T^{\rm singlet}/Z_T^{\rm nonsinglet} = 1 + O(\alpha_s^3) \approx 1$ where $a = \alpha_s/4\pi$ and n_f denotes the number of flavors. The largest disconnected contribution (off-diagonal elements $d_\Gamma^{ff'}$) is for the axial. In the $\{u-d, u+d, s\}$ basis, it is approximately 7% for the coarsest $a\approx 0.15$ fm ensemble and decreases to below 2% at the finest $a\approx 0.06$ fm ensemble.

The final factors used to renormalize the charges are given in Appendix B 5. Note the significant differences between results with the Z_1 versus the Z_2 strategies (defined in Appendix B 4) used to calculate Z_ψ. There is a similar pattern of differences between the three diagonal elements with $Z^{u-d,u-d} \approx Z^{u+d,u+d}$ that differ significantly from $Z^{s,s}$. This mass dependence is discussed in Appendix B 4 and our current understanding is, it is a discretization effect that in the final analysis is, to a large extent, taken care of in the continuum (CCFV) extrapolation of the renormalized charges. The mixing is $O(\alpha_s^2)$ in lattice perturbation theory [74], which would be larger than what the lattice data for the tensor operator given in Appendix B 5 suggests.

In Fig. 21, we show the data for Z_Γ in $\overline{\rm MS}$ scheme at 2 GeV for the $a06m310$ ensemble as a functions of μ along with fits using Eq. (B14). The results for the diagonal parts, for both Z_1 and Z_2, show a difference that vanishes in the continuum limit. The off-diagonal mixing elements $Z_\Gamma^{u+d,s}$ and $Z_\Gamma^{s,u+d}$ shown in the bottom two rows are all smaller than 1% and results with the Z_1 and Z_2 strategies essentially overlap.

One advantage of using RI-sMOM scheme for the scalar channel is the better convergence between two- and three-loop running and smaller deviation from unity in the

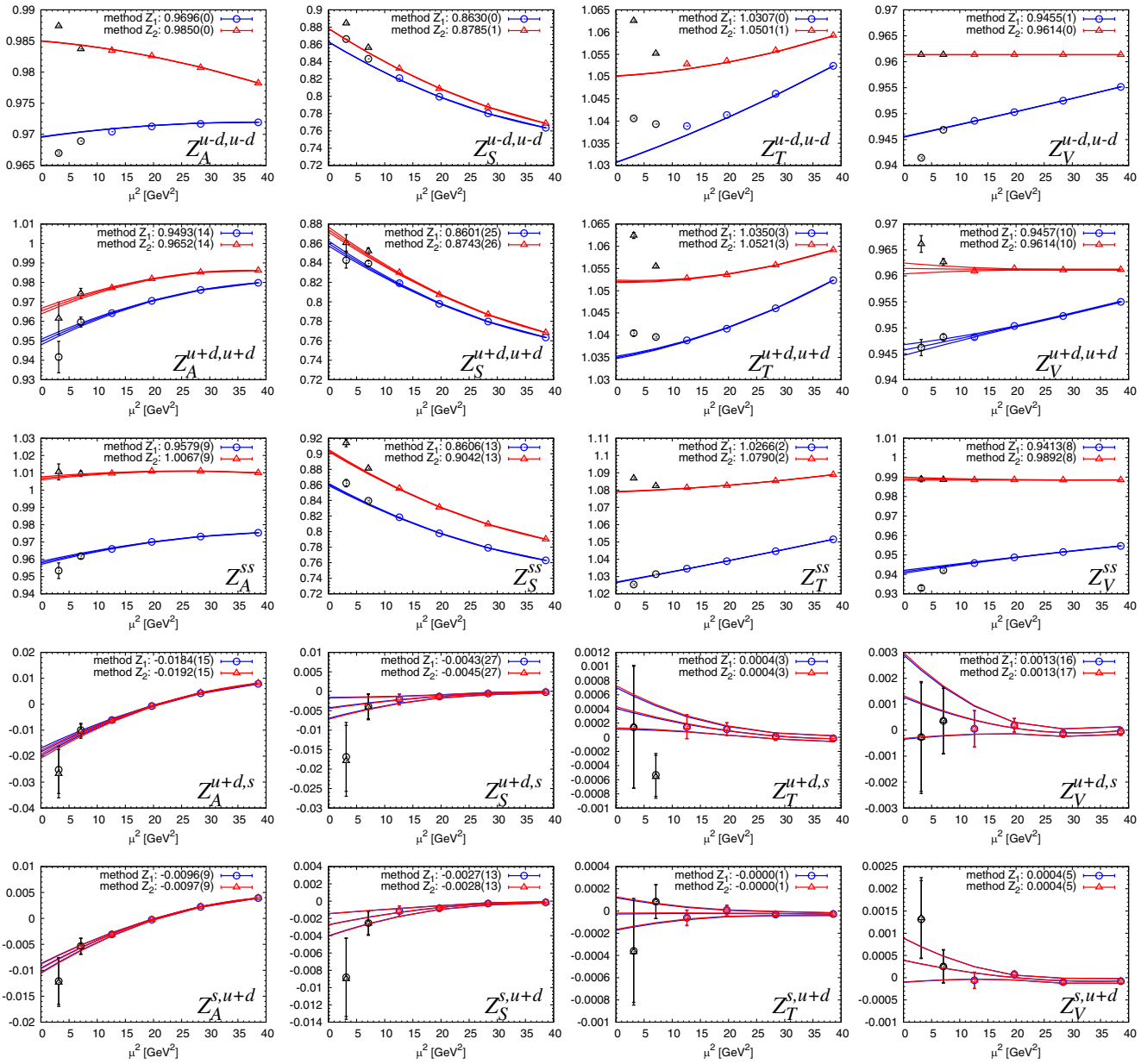


FIG. 21. Data for Z_Γ in $\overline{\text{MS}}$ scheme at 2 GeV on the a06m310 ensemble along with a quadratic fit versus μ^2 defined in Eq. (B14). Each panel compares results from the two different strategies, Z_1 (blue) and Z_2 (red). The four columns give results for the axial, scalar, tensor and vector operators, respectively. Each row represents one of the five nonzero matrix elements in the 3×3 matrix defining Z in the $\{u-d, u+d, s\}$ basis in Eq. (B10).

perturbative series for the matching factor compared to the RI-MOM scheme [10,66] as illustrated in Fig. 22.

To summarize, for our setup, the numerical results given in Appendix B 5 show that the off-diagonal terms and the $r_{\mathcal{O}} - 1$ factors are small.

4. Two renormalization strategies Z_1 and Z_2 defined by the choice of Z_ψ^q

To define the Z_1 and Z_2 renormalization strategies used, recall that the renormalization constants for the *isovector* bilinear operators in the RI scheme are given by

$$Z_\Gamma(p) = \frac{Z_\psi(p)}{c_\Gamma(p)} \quad \text{or} \quad Z_\psi(p) = c_\Gamma(p) Z_\Gamma(p), \tag{B17}$$

where p is the momentum insertion, Z_ψ is the renormalization constant for the fermion field, and c_Γ is the projected amputated connected three-point function calculated in Landau gauge as defined in Eq. (B6). Z_1 and Z_2 are defined by the two ways used to calculate Z_ψ.

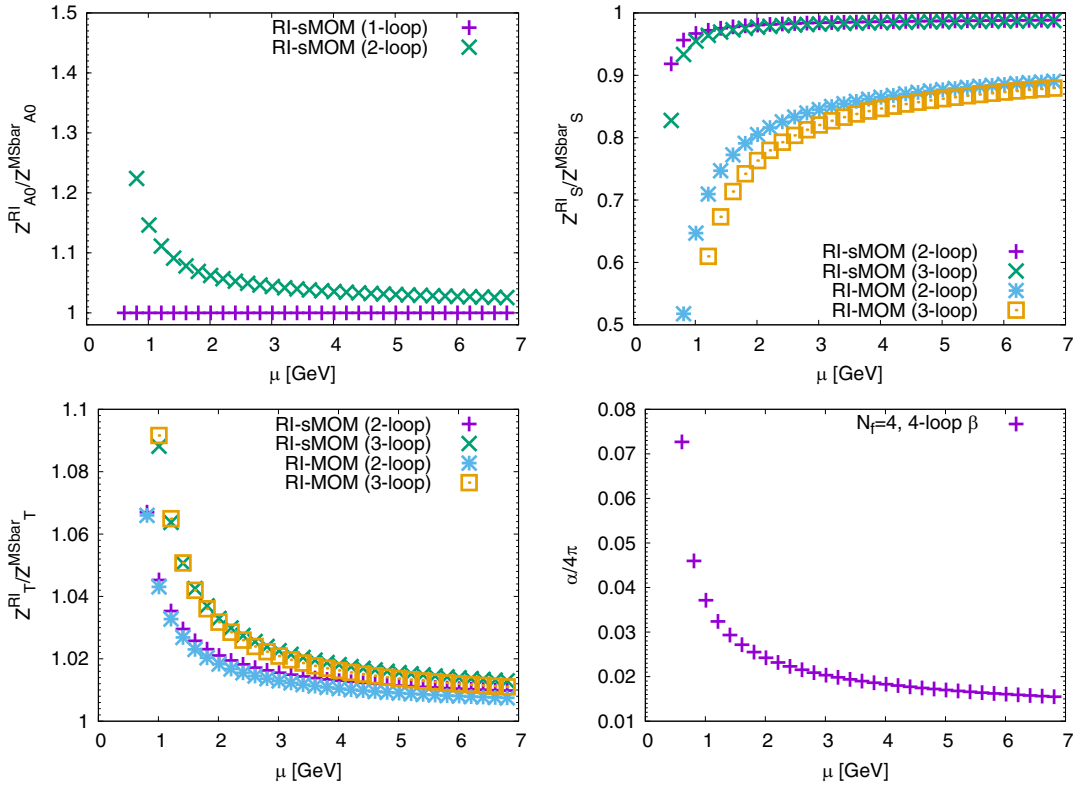


FIG. 22. Top left: matching factor $C^{\mathrm{RI-sMOM}\to\overline{\mathrm{MS}}} = Z^{\mathrm{RI-sMOM}}(\mu)/Z^{\overline{\mathrm{MS}}}(\mu)$ for the singlet axial current. It acquires a nontrivial dependence on the scale μ starting at two loops. For scalar and tensor operators, we compare the two- and three-loop matching factors for RI-sMOM $\to \overline{\mathrm{MS}}$ and RI-MOM $\to \overline{\mathrm{MS}}$. Bottom right: four-loop running of $\alpha/4\pi$ versus μ for the $N_f = 4$ theory used in this study.

(i) Z_1: The Z_ψ is calculated from the projected bare quark propagator

$$Z_\psi(p) = \frac{i}{12p^2}\mathrm{Tr}[S_B^{-1}(p)\not{p}] \tag{B18}$$

(ii) Z_2 calculated using the vector Ward identity (VWI), $Z_V g_V = 1$. Equation (B1) then becomes

$$Z_\psi^{\mathrm{VWI}}(p) = c_V(p)/g_V, \tag{B19}$$

where c_V is the projected amputated connected three-point function with insertion of the local vector operator within the quark state while the vector charge g_V is obtained from the insertion of the same operator within any, in principle, hadronic state, i.e., pion, nucleon, etc. We use the nucleon state.

These two strategies were used in Refs. [19,70] for *isovector* bilinear operators of light quarks, i.e., $g_\Gamma Z_\Gamma$ and $Z_\Gamma/Z_V \times g_\Gamma/g_V$. Later, they were called Z_1 and Z_2 in Ref. [12]. In Refs. [19,70] we showed that they have different behavior versus q^2 as the discretization effects are different in Z_ψ and Z_ψ^{VWI}, which are obtained from $S_B(p)$ and $c_\Gamma^V(p)$, respectively.[3] To within expected discretization errors, we checked

(i) $Z_V|_{Z_1} \times g_V^{l,\mathrm{bare}} = 1$ for m_l as shown in Table X. The deviation from unity decreases as $a \to 0$. When this relation is satisfied, renormalization using Z_1 and Z_2 should give consistent results.

(ii) Final continuum limit values of all the nucleon charges (and form factors), using Z_1 and Z_2 agree within the quoted errors [12].

This work extends the calculation to the heavier strange quark. The data in Table X show that the deviation of the renormalized g_V^s from unity is significantly larger. While this deviation for both the light and strange quarks goes to zero essentially linearly as $a \to 0$ as shown in Figs. 23 and 24, it is important to note that the discretization artifact is large and has a significant mass dependence.

We point out that these deviations are not due to incomplete removal of ESCs in the extraction of the isovector vector charge g_V. The data for the bare vector

[3]The $O(a)$ improvement for $S_B(p)$ is studied in Ref. [75], and $c_\Gamma^V(p)$ (off-shell improvement) is studied in Ref. [76].

TABLE X. Bare and the Z_1-renormalized vector charge for the light and strange quarks on the four ensembles. The nonperturbative calculations was done using the RI-sMOM scheme. The factor $Z_V^{\{l,s\}}|_{Z_1}$ is obtained using the quadratic extrapolation *Ansatz* given in Eq. (B14). The bare isovector vector charge $g_V^{\{l,s\},\text{bare}}$ is obtained from the forward matrix element within the nucleon ground state.

Ensemble	$g_V^{l,\text{bare}}$	$Z_V^l\|_{Z_1}$	$g_V^l\|_{Z_1}$	$g_V^{s,\text{bare}}$	$Z_V^s\|_{Z_1}$	$g_V^s\|_{Z_1}$
a15m310	1.0689(19)	0.86503(28)	0.925(2)	0.9845(3)	0.85690(18)	0.8436(3)
a12m220	1.0630(73)	0.90611(6)	0.963(7)	1.0007(3)	0.90048(4)	0.9011(3)
a09m220	1.0498(15)	0.92538(4)	0.971(1)	1.0053(1)	0.91608(3)	0.9209(1)
a06m310	1.0402(26)	0.94550(6)	0.984(2)	1.0116(3)	0.94110(4)	0.9520(3)

charge, i.e., the ratio plots versus $\{\tau, t\}$, are shown in Fig. 25. The ESCs are less than a percent, while the deviations in the data, shown in Table X, are a 2%–8% effect for even the light quarks.

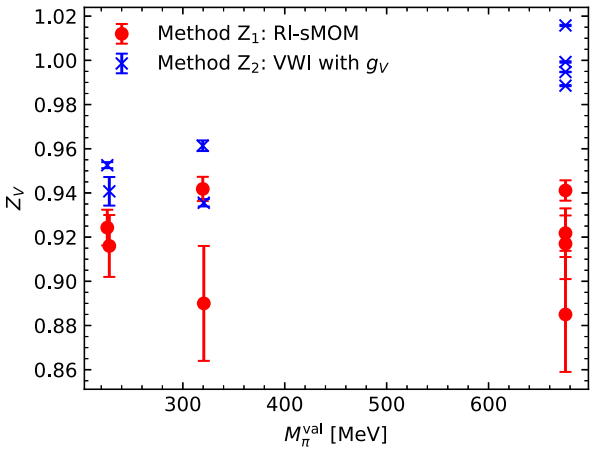


FIG. 23. Results for Z_V using the two strategies Z_1 and Z_2.

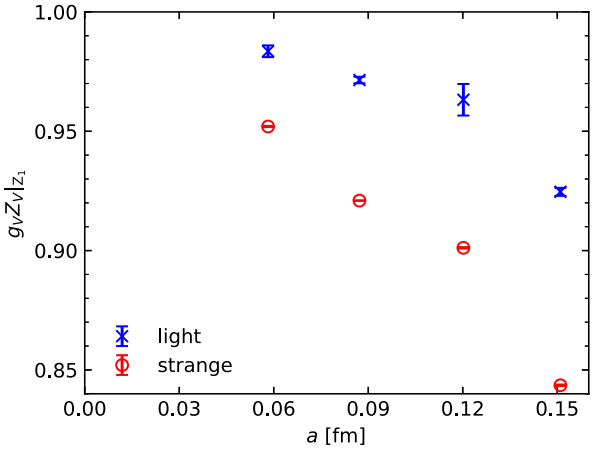


FIG. 24. Data for $g_V^f Z_V^f|_{Z_1}$, with the vector renormalization factor $Z_V^f|_{Z_1} = 1/c_V^f$, for flavor $f \in \{l, s\}$. See Eq. (B17) for details. The isovector vector charge $g_V^{\{l,s\}}$ is obtained from the forward matrix element within the nucleon ground state constructed using light and strange valence quark propagators respectively. The trend in the data is consistent with the VWI relation $g_V Z_V|_{Z_1} = 1$ being satisfied in the continuum limit.

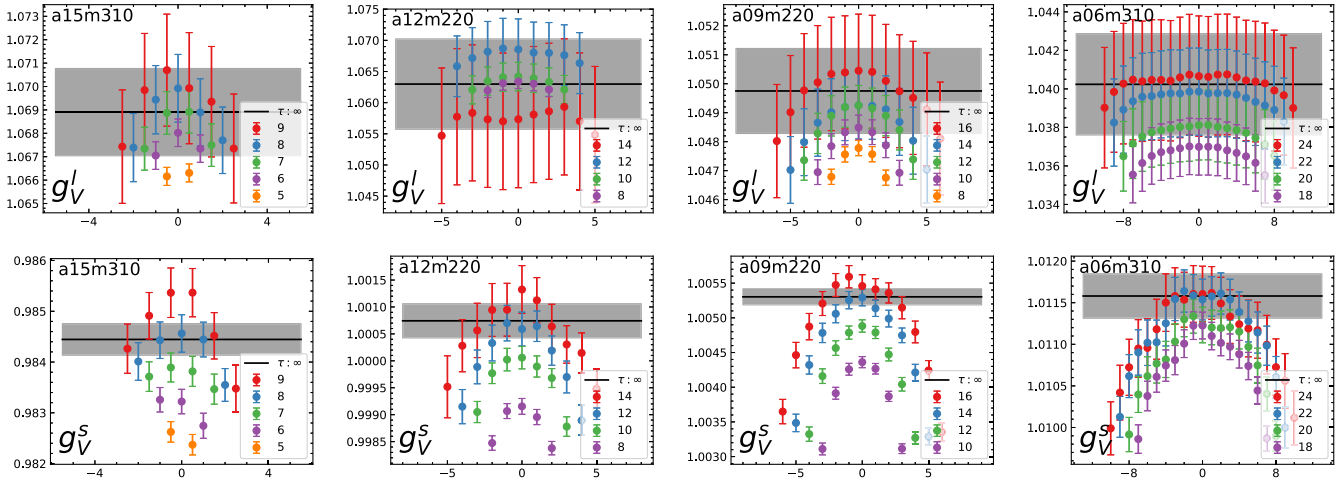


FIG. 25. Data for the nucleon vector charge g_V on four HISQ ensembles, $a15m310$, $a12m220$, $a09m220$, and $a06m310$, plotted from left to right. The top row is for the light valence quark with mass m_l and the bottom for the strange quark with mass m_s. The data at the largest three source-sink separations τ agree at the subpercent level. For the final result (gray band), we take the unweighted average over 4–10 data points centered about $t - \tau/2 = 0$ with the largest two τ. Residual ES effects are neglected.

5. Final results for the renormalization factors

The final renormalization factors in the $\overline{\text{MS}}$ scheme at 2 GeV, calculated using the $2+1$ theory in the flavor basis $f \in \{u-d, u+d, s\}$, are given below for the four ensembles, a15m310, a12m310, a09m310, and a06m310, the three charges, and the two renormalization methods, Z_1 and Z_2. These factors are the aggregate of the four steps described in Sec. B 3 and used to renormalize the bare charges for all the ensembles at a given lattice spacing a assuming their dependence on the quark masses is negligible compared to the other uncertainties.

$a \approx 0.15$ fm

$$Z_A|_{Z_1} = \begin{pmatrix} 0.9467(1) & 0 & 0 \\ 0 & 0.8905(21) & -0.0560(27) \\ 0 & -0.0269(11) & 0.9125(13) \end{pmatrix} \quad Z_A|_{Z_2} = \begin{pmatrix} 1.0222(3) & 0 & 0 \\ 0 & 0.9627(22) & -0.0647(28) \\ 0 & -0.0285(12) & 1.0803(14) \end{pmatrix} \tag{B20}$$

$$Z_S|_{Z_1} = \begin{pmatrix} 1.0034(2) & 0 & 0 \\ 0 & 0.9642(75) & -0.0323(75) \\ 0 & -0.0198(39) & 0.9806(38) \end{pmatrix} \quad Z_S|_{Z_2} = \begin{pmatrix} 1.0792(3) & 0 & 0 \\ 0 & 1.0381(81) & -0.0370(79) \\ 0 & -0.0208(42) & 1.1554(40) \end{pmatrix} \tag{B21}$$

$$Z_T|_{Z_1} = \begin{pmatrix} 0.8925(1) & 0 & 0 \\ 0 & 0.8930(6) & 0.0003(8) \\ 0 & 0.0001(3) & 0.8764(4) \end{pmatrix} \quad Z_T|_{Z_2} = \begin{pmatrix} 0.9653(2) & 0 & 0 \\ 0 & 0.9659(6) & 0.0004(8) \\ 0 & 0.0001(3) & 1.0393(4) \end{pmatrix} \tag{B22}$$

$a \approx 0.12$ fm

$$Z_A|_{Z_1} = \begin{pmatrix} 0.95705(4) & 0 & 0 \\ 0 & 0.9287(6) & -0.0283(11) \\ 0 & -0.0141(4) & 0.9386(4) \end{pmatrix} \quad Z_A|_{Z_2} = \begin{pmatrix} 0.9933(1) & 0 & 0 \\ 0 & 0.9642(6) & -0.0307(11) \\ 0 & -0.0143(4) & 1.0389(4) \end{pmatrix} \tag{B23}$$

$$Z_S|_{Z_1} = \begin{pmatrix} 0.9183(1) & 0 & 0 \\ 0 & 0.9163(43) & -0.0074(63) \\ 0 & -0.0010(24) & 0.9148(30) \end{pmatrix} \quad Z_S|_{Z_2} = \begin{pmatrix} 0.94423(4) & 0 & 0 \\ 0 & 0.9493(44) & -0.0080(64) \\ 0 & -0.0010(25) & 1.0119(31) \end{pmatrix} \tag{B24}$$

$$Z_T|_{Z_1} = \begin{pmatrix} 0.94254(5) & 0 & 0 \\ 0 & 0.9424(3) & 0.0003(5) \\ 0 & -0.0002(2) & 0.9358(2) \end{pmatrix} \quad Z_T|_{Z_2} = \begin{pmatrix} 0.97970(4) & 0 & 0 \\ 0 & 0.9792(3) & 0.0003(5) \\ 0 & -0.0002(2) & 1.0380(2) \end{pmatrix} \tag{B25}$$

$a \approx 0.09$ fm

$$Z_A|_{Z_1} = \begin{pmatrix} 0.96407(4) & 0 & 0 \\ 0 & 0.9356(17) & -0.0286(18) \\ 0 & -0.0155(9) & 0.9454(9) \end{pmatrix} \quad Z_A|_{Z_2} = \begin{pmatrix} 0.99252(4) & 0 & 0 \\ 0 & 0.9631(17) & -0.0307(18) \\ 0 & -0.0159(9) & 1.0251(10) \end{pmatrix} \tag{B26}$$

$$Z_S|_{Z_1} = \begin{pmatrix} 0.92167(5) & 0 & 0 \\ 0 & 0.9158(40) & -0.0067(40) \\ 0 & -0.0025(21) & 0.9141(21) \end{pmatrix} \quad Z_S|_{Z_2} = \begin{pmatrix} 0.9464(1) & 0 & 0 \\ 0 & 0.9419(42) & -0.0073(41) \\ 0 & -0.0025(22) & 0.9900(21) \end{pmatrix} \tag{B27}$$

$$Z_T|_{Z_1} = \begin{pmatrix} 0.98950(4) & 0 & 0 \\ 0 & 0.9892(6) & -0.0002(7) \\ 0 & 0.0002(3) & 0.9763(4) \end{pmatrix} \quad Z_T|_{Z_2} = \begin{pmatrix} 1.01847(4) & 0 & 0 \\ 0 & 1.0182(6) & -0.0002(7) \\ 0 & 0.0002(3) & 1.0592(4) \end{pmatrix} \tag{B28}$$

$a \approx 0.06$ fm

$$Z_A|_{Z_1} = \begin{pmatrix} 0.96958(5) & 0 & 0 \\ 0 & 0.9493(14) & -0.0184(15) \\ 0 & -0.0096(9) & 0.9579(9) \end{pmatrix} \quad Z_A|_{Z_2} = \begin{pmatrix} 0.98501(4) & 0 & 0 \\ 0 & 0.9652(14) & -0.0192(15) \\ 0 & -0.0097(9) & 1.0068(9) \end{pmatrix} \tag{B29}$$

$$Z_S|_{Z_1} = \begin{pmatrix} 0.86298(5) & 0 & 0 \\ 0 & 0.8601(25) & -0.0043(27) \\ 0 & -0.0027(13) & 0.8606(13) \end{pmatrix} \quad Z_S|_{Z_2} = \begin{pmatrix} 0.8785(1) & 0 & 0 \\ 0 & 0.8743(26) & -0.0045(27) \\ 0 & -0.0028(13) & 0.9042(13) \end{pmatrix} \tag{B30}$$

$$Z_T|_{Z_1} = \begin{pmatrix} 1.03069(5) & 0 & 0 \\ 0 & 1.0350(3) & 0.0004(3) \\ 0 & -0.0000(2) & 1.0266(2) \end{pmatrix} \quad Z_T|_{Z_2} = \begin{pmatrix} 1.0501(1) & 0 & 0 \\ 0 & 1.0521(3) & 0.0004(3) \\ 0 & -0.0000(2) & 1.0790(2) \end{pmatrix} \tag{B31}$$

[1] A. Bazavov, C. Bernard, J. Komijani, C. DeTar, L. Levkova, W. Freeman, S. Gottlieb, R. Zhou, U. M. Heller, J. E. Hetrick, J. Laiho, J. Osborn, R. L. Sugar, D. Toussaint, and R. S. Van de Water (MILC Collaboration), Phys. Rev. D **87**, 054505 (2013).

[2] R. Gupta, Y.-C. Jang, B. Yoon, H.-W. Lin, V. Cirigliano, and T. Bhattacharya, Phys. Rev. D **98**, 034503 (2018).

[3] H.-W. Lin, R. Gupta, B. Yoon, Y.-C. Jang, and T. Bhattacharya, Phys. Rev. D **98**, 094512 (2018).

[4] R. Gupta, B. Yoon, T. Bhattacharya, V. Cirigliano, Y.-C. Jang, and H.-W. Lin, Phys. Rev. D **98**, 091501 (2018).

[5] R. Gupta, S. Park, M. Hoferichter, E. Mereghetti, B. Yoon, and T. Bhattacharya, Phys. Rev. Lett. **127**, 242002 (2021).

[6] Y. Aoki *et al.* (Flavour Lattice Averaging Group (FLAG) Collaboration), arXiv:2411.04268.

[7] S. Park, T. Bhattacharya, R. Gupta, H.-W. Lin, S. Mondal, and B. Yoon, Proc. Sci., LATTICE2022 (**2023**) 118 [arXiv:2301.07890].

[8] S. Park, T. Bhattacharya, R. Gupta, H.-W. Lin, S. Mondal, and B. Yoon, Proc. Sci., LATTICE2023 (**2024**) 328 [arXiv:2401.00721].

[9] G. Martinelli, C. Pittori, C. T. Sachrajda, M. Testa, and A. Vladikas, Nucl. Phys. **B445**, 81 (1995).

[10] C. Sturm, Y. Aoki, N. H. Christ, T. Izubuchi, C. T. C. Sachrajda, and A. Soni, Phys. Rev. D **80**, 014501 (2009).

[11] Y.-C. Jang, R. Gupta, B. Yoon, and T. Bhattacharya, Phys. Rev. Lett. **124**, 072002 (2020).

[12] S. Park, R. Gupta, B. Yoon, S. Mondal, T. Bhattacharya, Y.-C. Jang, B. Joó, and F. Winter (Nucleon Matrix Elements (NME) Collaboration), Phys. Rev. D **105**, 054505 (2022).

[13] Y.-C. Jang, R. Gupta, T. Bhattacharya, B. Yoon, and H.-W. Lin, Phys. Rev. D **109**, 014503 (2024).

[14] H. Akaike, IEEE Trans. Autom. Control **19**, 716 (1974).

[15] T. Bhattacharya, V. Cirigliano, S. D. Cohen, R. Gupta, A. Joseph, H.-W. Lin, and B. Yoon (PNDME Collaboration), Phys. Rev. D **92**, 094511 (2015).

[16] A. Hasenfratz and F. Knechtli, Phys. Rev. D **64**, 034504 (2001).

[17] S. Gusken, U. Low, K. H. Mutter, R. Sommer, A. Patel, and K. Schilling, Phys. Lett. B **227**, 266 (1989).

[18] B. Yoon *et al.*, Phys. Rev. D **93**, 114506 (2016).

[19] B. Yoon *et al.*, Phys. Rev. D **95**, 074508 (2017).

[20] J. D. Bratt *et al.* (LHPC Collaboration), Phys. Rev. D **82**, 094502 (2010).

[21] G. S. Bali, S. Collins, and A. Schäfer, Comput. Phys. Commun. **181**, 1570 (2010).

[22] T. Blum, T. Izubuchi, and E. Shintani, Phys. Rev. D **88**, 094503 (2013).

[23] C. Thron, S. J. Dong, K. F. Liu, and H. P. Ying, Phys. Rev. D **57**, 1642 (1998).

[24] C. Michael, M. S. Foster, and C. McNeile (UKQCD Collaboration), Nucl. Phys. B, Proc. Suppl. **83–84**, 185 (2000).

[25] T. Bhattacharya, R. Gupta, W. Lee, S. R. Sharpe, and J. M. S. Wu, Phys. Rev. D **73**, 034504 (2006).

[26] R. G. Edwards and B. Joó (SciDAC, LHPC, UKQCD Collaborations), Nucl. Phys. B, Proc. Suppl. **140**, 832 (2005).

[27] M. A. Clark, R. Babich, K. Barros, R. C. Brower, and C. Rebbi, Comput. Phys. Commun. **181**, 1517 (2010).

[28] R. Babich, M. A. Clark, and B. Joo, *ACM/IEEE International Conference for High Performance Computing, Networking, Storage and Analysis, New Orleans* (2010), 10.1109/SC.2010.40.

[29] R. Babich, M. A. Clark, B. Joo, G. Shi, R. C. Brower, and S. Gottlieb, in *SC11 International Conference for High Performance Computing, Networking, Storage and Analysis Seattle, Washington, 2011* (2011), arXiv:1109.2935.

[30] J. Brannick, R. C. Brower, M. A. Clark, J. C. Osborn, and C. Rebbi, Phys. Rev. Lett. **100**, 041601 (2008).
[31] R. Babich, J. Brannick, R. C. Brower, M. A. Clark, T. A. Manteuffel *et al.*, Phys. Rev. Lett. **105**, 201602 (2010).
[32] J. C. Osborn, R. Babich, J. Brannick, R. C. Brower, M. A. Clark *et al.*, Proc. Sci., LATTICE2010 (**2010**) 037 [arXiv:1011.2775].
[33] M. A. Clark, B. Joó, A. Strelchenko, M. Cheng, A. Gambhir, and R. Brower, *ACM/IEEE International Conference for High Performance Computing, Networking, Storage and Analysis, Salt Lake City, Utah* (2016), 10.1109/SC.2010.40.
[34] H. W. Hamber, E. Marinari, G. Parisi, and C. Rebbi, Nucl. Phys. **B225**, 475 (1983).
[35] G. P. Lepage, in *Boulder ASI 1989:97-120* (World Scientific, Singapore, 1989), pp. 97–120.
[36] O. Bär, Phys. Rev. D **92**, 074504 (2015).
[37] W. I. Jay and E. T. Neil, Phys. Rev. D **103**, 114502 (2021).
[38] O. Bär, Phys. Rev. D **94**, 054505 (2016).
[39] C. Alexandrou, S. Bacchio, J. Finkenrath, C. Iona, G. Koutsou, Y. Li, and G. Spanoudes, Phys. Rev. D **111**, 054505 (2025).
[40] D. Djukanovic, H. Meyer, K. Ottnad, G. von Hippel, J. Wilhelm, and H. Wittig, Proc. Sci., LATTICE2019 (**2019**) 158 [arXiv:1911.01177].
[41] J. Liang, Y.-B. Yang, T. Draper, M. Gong, and K.-F. Liu, Phys. Rev. D **98**, 074505 (2018).
[42] Sz. Borsanyi, Z. Fodor, C. Hoelbling, L. Lellouch, K. K. Szabo, C. Torrero, and L. Varnhorst (BMWc Collaboration), arXiv:2007.03319.
[43] C. Alexandrou, V. Drach, K. Jansen, C. Kallidonis, and G. Koutsou, Phys. Rev. D **90**, 074501 (2014).
[44] A. Agadjanov, D. Djukanovic, G. von Hippel, H. B. Meyer, K. Ottnad, and H. Wittig, Phys. Rev. Lett. **131**, 261902 (2023).
[45] G. S. Bali, S. Collins, P. Georg, D. Jenkins, P. Korcyl, A. Schäfer, E. E. Scholz, J. Simeth, W. Söldner, and S. Weishäupl (RQCD Collaboration), J. High Energy Phys. 05 (2023) 035.
[46] Y.-B. Yang, A. Alexandru, T. Draper, J. Liang, and K.-F. Liu (χQCD Collaboration), Phys. Rev. D **94**, 054503 (2016).
[47] S. Dürr, Z. Fodor, C. Hoelbling, S. D. Katz, S. Krieg, L. Lellouch, T. Lippert, T. Metivet, A. Portelli, K. K. Szabo, C. Torrero, B. C. Toth, and L. Varnhorst (Budapest-Marseille-Wuppertal Collaboration), Phys. Rev. Lett. **116**, 172001 (2016).
[48] M. Hoferichter, J. R. de Elvira, B. Kubis, and U.-G. Meißner, Phys. Lett. B **843**, 138001 (2023).
[49] J. Ruiz de Elvira, M. Hoferichter, B. Kubis, and Ulf-G. Meißner, J. Phys. G **45**, 024001 (2018).
[50] M. Hoferichter, J. Ruiz de Elvira, B. Kubis, and Ulf-G. Meißner, Phys. Rev. Lett. **115**, 092301 (2015).
[51] Y.-H. Chen, D.-L. Yao, and H. Q. Zheng, Phys. Rev. D **87**, 054019 (2013).
[52] J. M. Alarcón, J. Martin Camalich, and J. A. Oller, Phys. Rev. D **85**, 051503(R) (2012).
[53] C. McNeile, A. Bazavov, C. T. H. Davies, R. J. Dowdall, K. Hornbostel, G. P. Lepage, and H. D. Trottier, Phys. Rev. D **87**, 034503 (2013).
[54] P. M. Junnarkar and A. Walker-Loud, Phys. Rev. D **87**, 114510 (2013).
[55] D. Toussaint and W. Freeman (MILC Collaboration), Phys. Rev. Lett. **103**, 122002 (2009).
[56] M. Hoferichter, J. Ruiz de Elvira, B. Kubis, and Ulf-G. Meißner, Phys. Rep. **625**, 1 (2016).
[57] C. Adolph *et al.* (COMPASS Collaboration), Phys. Lett. B **753**, 18 (2016).
[58] H.-W. Lin, W. Melnitchouk, A. Prokudin, N. Sato, and H. Shows, Phys. Rev. Lett. **120**, 152502 (2018).
[59] M. Radici and A. Bacchetta, Phys. Rev. Lett. **120**, 192001 (2018).
[60] Z. Ye, N. Sato, K. Allada, T. Liu, J.-P. Chen, H. Gao, Z.-B. Kang, A. Prokudin, P. Sun, and F. Yuan, Phys. Lett. B **767**, 91 (2017).
[61] Y. Aoki *et al.* (Flavour Lattice Averaging Group (FLAG) Collaboration), Eur. Phys. J. C **82**, 869 (2022).
[62] B. A. Kniehl and O. L. Veretin, Phys. Lett. B **804**, 135398 (2020).
[63] P. A. Baikov, K. G. Chetyrkin, and J. H. Kühn, J. High Energy Phys. 10 (2014) 076.
[64] J. A. Gracey, Phys. Rev. D **106**, 085008 (2022).
[65] J. A. Gracey, Eur. Phys. J. C **71**, 1567 (2011).
[66] K. G. Chetyrkin and A. Retey, Nucl. Phys. **B583**, 3 (2000).
[67] J. A. Gracey, Phys. Lett. B **488**, 175 (2000).
[68] J. A. Gracey, Phys. Rev. D **102**, 036002 (2020).
[69] J. I. Skullerud and A. G. Williams, Nucl. Phys. B, Proc. Suppl. **83–84**, 209 (2000).
[70] T. Bhattacharya, V. Cirigliano, S. D. Cohen, R. Gupta, H.-W. Lin, and B. Yoon, Phys. Rev. D **94**, 054508 (2016).
[71] J. Green, N. Hasan, S. Meinel, M. Engelhardt, S. Krieg, J. Laeuchli, J. Negele, K. Orginos, A. Pochinsky, and S. Syritsyn, Phys. Rev. D **95**, 114502 (2017).
[72] S. A. Larin, Phys. Lett. B **303**, 113 (1993).
[73] L. Chen and M. Czakon, J. High Energy Phys. 01 (2022) 187.
[74] M. Constantinou, M. Hadjiantonis, H. Panagopoulos, and G. Spanoudes, Phys. Rev. D **94**, 114513 (2016).
[75] T. Bhattacharya, R. Gupta, and W. Lee, Nucl. Phys. B, Proc. Suppl. **94**, 595 (2001).
[76] T. Bhattacharya, R. Gupta, and W. Lee, Nucl. Phys. B, Proc. Suppl. **106–107**, 786 (2002).